Upstream open reading frames control PLK4 translation and centriole duplication in primordial germ cells

Thao P. Phan,[1] Christina A. Boatwright,[1] Chelsea G. Drown,[1] Marnie W. Skinner,[2,3] Margaret A. Strong,[1] Philip W. Jordan,[2,3] and Andrew J. Holland[1]

[1]Department of Molecular Biology and Genetics, Johns Hopkins University School of Medicine, Baltimore, Maryland 21205, USA; [2]Department of Biochemistry and Molecular Biology, Bloomberg School of Public Health, Johns Hopkins University, Baltimore, Maryland 21205, USA; [3]Department of Biochemistry and Molecular Biology, Uniformed Services University of the Health Sciences, Bethesda, Maryland 20814, USA

Centrosomes are microtubule-organizing centers comprised of a pair of centrioles and the surrounding pericentriolar material. Abnormalities in centriole number are associated with cell division errors and can contribute to diseases such as cancer. Centriole duplication is limited to once per cell cycle and is controlled by the dosage-sensitive Polo-like kinase 4 (PLK4). Here, we show that PLK4 abundance is translationally controlled through conserved upstream open reading frames (uORFs) in the 5′ UTR of the mRNA. *Plk4* uORFs suppress *Plk4* translation and prevent excess protein synthesis. Mice with homozygous knockout of *Plk4* uORFs (*Plk4*$^{\Delta u/\Delta u}$) are viable but display dramatically reduced fertility because of a significant depletion of primordial germ cells (PGCs). The remaining PGCs in *Plk4*$^{\Delta u/\Delta u}$ mice contain extra centrioles and display evidence of increased mitotic errors. PGCs undergo hypertranscription and have substantially more *Plk4* mRNA than somatic cells. Reducing *Plk4* mRNA levels in mice lacking *Plk4* uORFs restored PGC numbers and fully rescued fertility. Together, our data uncover a specific requirement for uORF-dependent control of PLK4 translation in counterbalancing the increased *Plk4* transcription in PGCs. Thus, uORF-mediated translational suppression of PLK4 has a critical role in preventing centriole amplification and preserving the genomic integrity of future gametes.

[*Keywords*: centriole amplification; Polo-like kinase 4; primordial germ cell; translational regulation; upstream open reading frame]

Supplemental material is available for this article.

Received March 27, 2022; revised version accepted June 9, 2022.

Centrioles are microtubule-based organelles that recruit a surrounding pericentriolar material (PCM) to form a centrosome (Wang and Stearns 2018). As microtubule-organizing centers, centrosomes have central roles in maintaining cell shape, mediating subcellular trafficking, and regulating chromosome segregation during cell division (Nigg and Holland 2018; Ryniawec and Rogers 2021). In noncycling cells, centrioles function as basal bodies that template the assembly of cilia and flagella (Breslow and Holland 2019). To carry out these functions, centriole structure and copy number must be tightly controlled. Extra copies of centrioles are frequently observed in human cancers, where they contribute to genome instability and drive invasive phenotypes (Levine and Holland 2018). In addition, mutations in centriole genes are linked to growth retardation syndromes and microcephaly (Chavali et al. 2014; Jayaraman et al. 2018; Phan and Holland 2021).

Cycling cells couple centriole biogenesis with cell cycle progression. At the start of the cell cycle, a cell contains a pair of parent centrioles, each of which produces a single new procentriole during S phase. Procentriole assembly is controlled by the conserved central regulator Polo-like kinase 4 (PLK4) (Bettencourt-Dias et al. 2005; Habedanck et al. 2005). PLK4 is recruited to the base of the parent centriole by its centriole receptors, CEP152 and CEP192 (Cizmecioglu et al. 2010; Hatch et al. 2010; Kim et al. 2013; Sonnen et al. 2013; Park et al. 2014). At G1–S transition, PLK4 transforms from a ring-like localization to a single focus on the wall of the parent centriole, where PLK4 catalyzes reactions required for the initiation of procentriole assembly (Sonnen et al. 2012; Kim et al. 2013; Ohta et al. 2014; Dzhindzhev et al. 2017).

Corresponding author: aholland@jhmi.edu
Article published online ahead of print. Article and publication date are online at http://www.genesdev.org/cgi/doi/10.1101/gad.349604.122.

Control of centriole biogenesis is extremely sensitive to the abundance of PLK4. Decreased levels of PLK4 lead to a failure of centriole duplication, while modest increases in PLK4 abundance drive centriole amplification that can lead to mitotic errors and contribute to tumorigenesis in mice (Bettencourt-Dias et al. 2005; Habedanck et al. 2005; Coelho et al. 2015; Serçin et al. 2016; Levine et al. 2017). Several E3 ligases have been shown to ubiquitinate and degrade PLK4, explaining the short half-life and low cellular abundance of the protein (Cunha-Ferreira et al. 2009; Rogers et al. 2009; Cajanek et al. 2015). In one central form of regulation, the abundance of PLK4 is tightly controlled by a negative feedback loop where the dimeric kinase cross-phosphorylates in *trans* to mark itself for ubiquitination by the SCF^{BTrCP} E3 ubiquitin ligase (Cunha-Ferreira et al. 2009, 2013; Rogers et al. 2009; Guderian et al. 2010; Holland et al. 2010, 2012; Klebba et al. 2013). Ubiquitinated PLK4 is subsequently degraded by the proteasome, linking PLK4 stability to its kinase activity. In addition to stringent post-translational control of protein abundance, PLK4 levels are also modulated by cell cycle-regulated transcription and post-transcriptionally controlled by the binding of microRNAs to the 3′ UTR of the mRNA (Ledoux et al. 2013; Fischer et al. 2014; Lee et al. 2014; Fan et al. 2015; Bao et al. 2018; Zhang et al. 2019).

Upstream open reading frames (uORFs) are short open reading frames with a translation initiation codon located in the 5′ untranslated region (UTR) of an mRNA. Ribosomes scanning from the 5′ cap of an mRNA initiate translation at the first encountered start codon that has an optimal initiation context. For translation to initiate at the main ORF located downstream, the ribosome must either skip translation of the uORF (a process known as "leaky" scanning) or resume scanning and reinitiate translation after producing the uORF-encoded peptide (Morris and Geballe 2000; Kozak 2002; Barbosa et al. 2013). The probability of translation reinitiation downstream from uORF elements depends on several uORF-related features, including their translation initiation contexts, their length, and the intercistronic distance (Luukkonen et al. 1995; Kozak 2001; Pöyry et al. 2004). Nevertheless, the presence of uORFs in the 5′ UTR generally reduces the translation efficiency of the main ORF. Although uORFs often constitutively repress the translation of the coding sequence of a gene, there are also examples where multiple uORFs allow increased translation initiation of a gene in response to altered environmental conditions (Baird et al. 2014; Andreev et al. 2015; Gao et al. 2015). A major example of this regulation is following the activation of the integrated stress response (ISR) (Lu et al. 2004; Vattem and Wek 2004). The ISR is activated by various stresses and culminates in phosphorylation of the α subunit of the translation initiation factor eIF2. Phosphorylation of eIF2α leads to a decrease in general mRNA translation, but specifically up-regulates the translation of select mRNAs containing multiple uORFs. In the case of the transcription factor ATF4, eIF2α phosphorylation delays translational reinitiation, allowing ribosomes that translate uORF1 to bypass translation of an inhibitory uORF2 and reinitiate translation at the *ATF4*-coding region (Harding et al. 2000). The presence of uORFs is enriched among classes of genes involved in cell growth and differentiation (Kozak 1987, 1991; Ye et al. 2015). However, although uORFs have been widely studied in cultured cell lines, few studies have examined the physiological relevance of uORF-mediated translational control in the context of a multicellular organism.

Here we demonstrate that translation of PLK4 is controlled by uORFs in the 5′ UTR of the *PLK4* mRNA. uORFs are conserved among vertebrate *PLK4* transcripts and suppress translation of PLK4 protein. Using genetically engineered mice, we discovered that *PLK4* uORFs are required to limit PLK4 levels and formation of excess centriole numbers specifically in primordial germ cells (PGCs), the precursors of future gametes. Our data reveal a novel pathway for controlling PLK4 abundance and uncover a critical role of uORF-mediated control of translation during gametogenesis.

Results

uORFs suppress PLK4 translation

Using publicly available profiling data for elongating ribosomes, we identified two uORFs in the 5′ untranslated region (UTR) of the human *PLK4* mRNA: The 5′-proximal uORF1 encodes 30 amino acids, while uORF2 encodes 74 amino acids and overlaps out of frame with the *PLK4*-coding region (Fig. 1A). Ribosome profiling of initiating ribosomes showed a strong peak at the ATG of uORF1, indicating that this is the primary site of translational initiation in the *PLK4* mRNA (Fig. 1A). uORF1 is conserved across vertebrates, while uORF2 is present in mammals but is predicted to be absent or have a different configuration in some nonmammalian vertebrates (Supplemental Fig. S1A). The amino acid sequences encoded by uORF1 and uORF2 are poorly conserved, suggesting that the uORF-encoded peptides do not have functional roles (Supplemental Fig. S1B,C).

To confirm that the human *PLK4* uORFs are translated, we generated reporter constructs with EGFP positioned immediately downstream from the ATG translation initiation codon for PLK4, uORF1, or uORF2 (Fig. 1B). The reporter constructs were integrated at a single genomic locus in the pseudodiploid human colon cancer Flp-In TRex-DLD-1 cell line. The mRNA expression levels for all reporters were similar (Fig. 1C). Analysis of EGFP expression levels by flow cytometry showed that uORF1 was highly translated, while expression of uORF2 was barely detectable (Fig. 1D). This is consistent with the data from ribosome profiles showing higher density of initiating ribosomes at uORF1 compared with uORF2 (Fig. 1A). We reasoned that ribosomes that translate uORF1 would be unable to reinitiate translation at uORF2 due to the short distance (13 bp) between the uORF1 stop codon and the start of uORF2. Instead, ribosomes that translate uORF1 are likely to reinitiate translation with a reduced probability at the AUG of *PLK4*. Consistent with the idea that uORF1 prevents translation of

uORF2, mutating the start codon of uORF1 (from AUG to AUA) increased the production of uORF2 EGFP by 15-fold (Fig. 1D). Furthermore, mutation of both uORF1 and uORF2 translation initiation codons (referred to as uORFs mut) led to a 16.5-fold increase in the level of EGFP production from the *PLK4* start codon. We conclude that

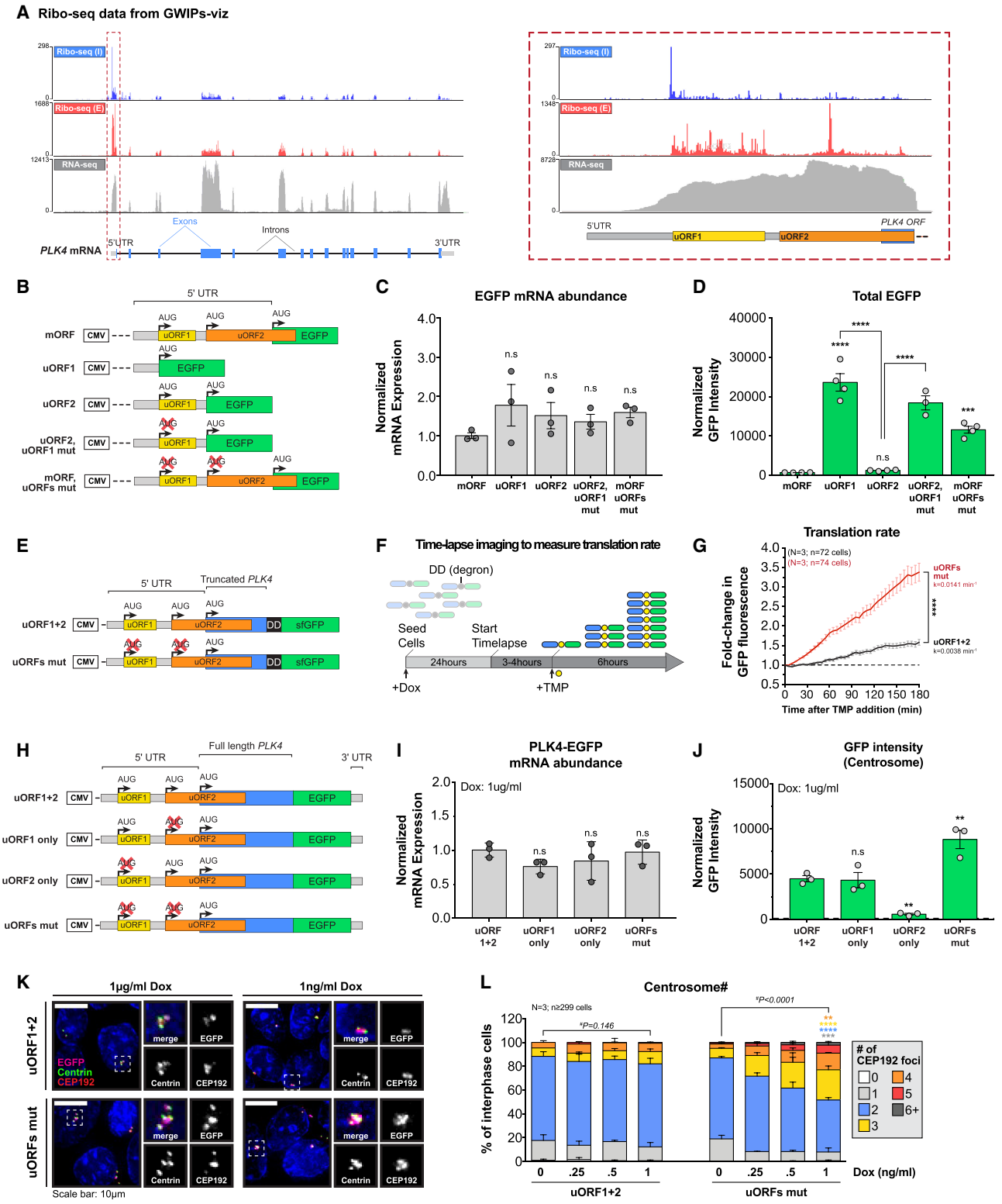

Figure 1. *See legend on following page.*

uORFs in the 5′ UTR of human *PLK4* strongly suppress translation initiation at the *PLK4* start codon.

To determine the role of uORFs in regulating *PLK4* expression, we generated a set of reporters that was comprised of the *PLK4* 5′ UTR with full-length uORF1 and uORF2 and the first 48 amino acids of the PLK4 protein linked to EGFP (Supplemental Fig. S1D). The wild-type 5′ UTR of the human *PLK4* mRNA (referred to as uORF1+2) allowed for minimal EGFP expression. Mutation of uORF2 (referred to as uORF1 only) slightly increased reporter expression. Meanwhile, mutation of the uORF1 start codon (referred to as uORF2 only) reduced EGFP to background levels (Supplemental Fig. S1E). This indicates that preventing uORF1 translation promotes translation of uORF2, which in turn blocks translation initiation of PLK4. Mutation of both uORF1 and uORF2 start codons (referred to as uORFs mut) resulted in an ∼9.5-fold increase in the level of EGFP produced without altering the mRNA levels of the transgene (Supplemental Fig. S1E,F). Translational suppression by uORFs was shown to be conserved in mouse, chicken, and zebrafish *PLK4* genes (Supplemental Fig. S1G–I). Thus, we conclude that uORFs function as conserved repressors of *PLK4* expression.

Next, we wanted to directly test how uORFs impact the translation rate of PLK4. To this end, we generated fluorescent reporter constructs comprised of the PLK4 5′ UTR and the first 48 amino acids of the PLK4 protein linked to NLS-sfGFP carrying an inducible degron (Fig. 1E; Iwamoto et al. 2010; Han et al. 2014). This led to the continuous degradation of the truncated PLK4-sfGFP protein until the stabilizer trimethoprim (TMP) was added. A wild-type or uORFs mut version of the reporter was integrated into a DLD-1 cell line that stably expresses nuclear PCNA-iRFP. The cell lines were monitored by live-cell imaging for 3 h after TMP addition and the translation rate was calculated based on the fold change in sfGFP expression (Fig. 1F). The uORFs mut reporter mRNA translated sfGFP at an ∼3.5-fold higher rate than the uORF1+2 mRNA, demonstrating that uORFs serve to dampen translation initiation from the start codon of the *PLK4* mRNA (Fig. 1G).

Finally, to test the role of uORFs in controlling centrosomal PLK4 abundance and centriole duplication, we generated a series of reporters containing a Dox-inducible full-length *PLK4* ORF fused to EGFP flanked by the *PLK4* 5′ and 3′ UTRs (Fig. 1H). All four of the constructs analyzed (uORF1+2, uORF1, uORF2, and uORFs mut) had similar mRNA levels (Fig. 1I). Consistent with prior observations, mutation of the start codon of uORF2 minimally impacted the level of centrosomal PLK4-EGFP, while loss of uORF1 dramatically suppressed PLK4-EGFP production (Fig. 1J). Mutation of both uORFs increased the level of PLK4-EGFP at centrosomes by approximately twofold, an increase that was substantially less than that observed with the truncated PLK4 reporter lacking both uORFs (Supplemental Fig. S1E). This difference may be due to the autocatalytic self-degradation of PLK4-EGFP that is further enhanced when the protein is concentrated at the centrosome.

Figure 1. uORFs suppress translation of PLK4. (*A*) Diagram of the human PLK4 transcript (*left*) with a zoomed-in view of the 5′ UTR (*right*). Ribo-seq ([I] initiating ribosome, [E] elongating ribosome) and RNA-seq (from GWIPs-viz database) are aligned to the transcript, highlighting regions where Ribo-seq reads correspond to uORF1 and uORF2. Specifically, the data were generated from various human cell lines. Initiating ribosomes were stalled using harringtonine or actimidomycin, and elongating ribosomes were frequently stalled using cyclohexamide (for specific methods used for each study, refer to https://gwips.ucc.ie). (*B*) Diagram showing fluorescent reporters used to measure the expression level of uORF1, uORF2, and PLK4 (human). The start codons of uORF1 and/or uORF2 were mutated from ATG to ATA (AUG to AUA in the mRNA) where indicated. (*C*) Graph showing mRNA abundance from DLD-1 Flp-In cells expressing reporters in *B* as measured by qRT-PCR 24 h following induction with 1 µg/mL Dox. $N = 3$ biological replicates, each with technical triplicate; one-way ANOVA with post-hoc analysis. (*D*) Graph showing GFP intensity from DLD-1 Flp-In cells expressing reporters in *B* as measured by flow cytometry 24 h following induction with 1 µg/mL Dox. Signal from a nonfluorescent control cell line was set to 100 and used for normalization. $N \geq 3$; one-way ANOVA with post-hoc analysis. (*E*) Diagram showing fluorescent reporters used to measure translation rate of a truncated N-terminal fragment of human PLK4 (48 amino acids) fused to a superfolder GFP fluorescent tag. Where indicated, the uORF1 and uORF2 start codons were mutated from ATG to ATA. (DD) ecDHFR degron, (sfGFP-NLS) superfolder GFP-tagged with a nuclear localization signal (NLS). (*F*) Schematic of the time-lapse experimental setup to measure translation rate of PLK4 using reporters from *E*. Dox (1 µg/mL) was added 24 h prior to the imaging session to induce transcription of the reporter. The next day, cells were filmed for ∼3 h before the addition of TMP, which allowed the sfGFP-NLS signal to accumulate over time. (*G*) Quantification of PLK4 translation rate over time of DLD-1 Flp-In cells expressing reporters in *E*. Translation rate was calculated as the slope of the normalized GFP signal plotted against time starting at the time of TMP addition. $N = 3$ biological replicates, $n \geq 72$ cells; linear regression analysis. (*H*) Diagram showing fluorescent reporters used to measure the expression level of the full-length PLK4 transcript (human). The uORF1 and uORF2 start codons were mutated from ATG to ATA where indicated. (*I*) Graph showing mRNA abundance from DLD-1 Flp-In cells expressing the human PLK4-EGFP reporters in *H* as measured by qRT-PCR 48 h following induction with 1 µg/mL Dox. $N = 3$ biological replicates, each with technical triplicate; one-way ANOVA with post-hoc analysis. (*J*) Quantification of human PLK4-EGFP fluorescent intensity at the centrosome from DLD-1 Flp-In cells expressing the reporters shown in *H* 48 h following induction with 1 µg/mL Dox. Signal from nonfluorescent control cell line, represented by a black dashed line, was set to 100 and used for normalization. $N = 3$ biological replicates; one-way ANOVA with post-hoc analysis. (*K*) Representative immunofluorescent images of DLD-1 Flp-In cells expressing human PLK4-EGFP reporters in *H* 48 h following induction with 1 µg/mL Dox (*left*) or 1 ng/mL Dox (*right*). Cells expressing PLK4-EGFP (magenta) were stained with antibodies against centrin (green), CEP192 (red), and DAPI (blue). *Insets* show zoomed-in views of representative centrosome foci. Scale bar, 10 µm. (*L*) Quantification of the number of CEP192 foci in interphase DLD-1 cells expressing human PLK4-EGFP reporters from *H* 48 h following induction with varying concentrations of Dox, $N = 3$ biological replicates, $n \geq 299$ cells. (#) χ^2 test, (*) post-hoc analysis. All data represent the means ± SEM. (**) $P < 0.01$, (***) $P < 0.001$, (****) $P < 0.0001$, (n.s) not significant ($P > 0.05$). (*N*) Number of biological replicates, (*n*) number of cells analyzed.

To determine whether uORFs can limit PLK4-driven centriole overduplication, we titrated the overexpression of uORF1+2 or uORFs mut PLK4-EGFP transgenes using different concentrations of Dox. The degree of centrosome amplification remained low (12%–18%) in the uORF1+2 reporter cell line across the range of Dox concentrations tested (0.25–1 ng/mL). However, the same concentrations of Dox drove a gradual increase (28%–48%) in the frequency of uORFs mut cells with centrosome amplification (Fig. 1K,L). Together, these data show that uORFs can act to limit centrosome amplification when the levels of *PLK4* mRNA are increased.

Removal of PLK4 *uORFs leads to specific defects in the reproductive system*

To test the physiological role of PLK4 uORFs, we generated mice with a $Plk4^{\Delta u}$ allele in which the start codons of *Plk4* uORF1 and uORF2 were mutated from ATG to ATA (Fig. 2A). Previous studies have shown that overexpression of PLK4 during mouse embryogenesis causes neonatal lethality, while overexpression of PLK4 postnatally drives centrosome amplification and spontaneous tumorigenesis. However, both $Plk4^{+/\Delta u}$ and $Plk4^{\Delta u/\Delta u}$ animals were produced at the expected Mendelian frequency and showed no evidence of increased tumor development by 8–9 mo of age (Fig. 2B; Supplemental Fig. S2C). Analysis of centriole number in tissues from 8- to 12-wk-old $Plk4^{+/+}$, $Plk4^{+/\Delta u}$, and $Plk4^{\Delta u/\Delta u}$ animals carrying a centrin-GFP transgene showed no increase in centriole copy number across several cell types, including intestinal plasma cells, splenocytes, and keratinocytes in animals with the $Plk4^{\Delta u}$ allele (Fig. 2C–E). We also did not observe centriole copy number aberrations in specialized cells such as polyploid hepatocytes and multiciliated ependymal cells (Supplemental Fig. S2A,B). In addition, histological analysis of multiple somatic tissues revealed no pathology in 8- to 9-mo-old $Plk4^{+/\Delta u}$ or $Plk4^{\Delta u/\Delta u}$ animals (Supplemental Fig. S2C,D).

Surprisingly, we found that $Plk4^{\Delta u/\Delta u}$ animals exhibited consistent defects in both male and female reproductive organs. Specifically, male and female $Plk4^{\Delta u/\Delta u}$ animals had significantly smaller testes and ovaries, respectively (Fig. 2F–H). Furthermore, histological sections from 8- to 9-mo-old $Plk4^{\Delta u/\Delta u}$ testes revealed patches of seminiferous tubules that were devoid of sperm, while the ovaries from 8-mo-old female $Plk4^{\Delta u/\Delta u}$ mice were atrophied and lacked any evidence of oocytes. Thus, our comprehensive analysis of $Plk4^{\Delta u/\Delta u}$ mice indicates that *Plk4* uORFs have an important and unique role in gametogenesis.

Loss of Plk4 *uORFs leads to germ cell depletion and reduced fertility*

To test the fertility of $Plk4^{\Delta u/\Delta u}$ animals, we paired 4- to 5-wk-old male or female mice with wild-type animals and monitored their breeding performance for 6 mo. While most $PLK4^{+/+}$ and $Plk4^{+/\Delta u}$ animals generated at least one litter of approximately seven to nine pups by 12 wk of age, the majority of $Plk4^{\Delta u/\Delta u}$ animals failed to produce offspring (Fig. 3A,B; Supplemental Fig. S3A,B). In the rare instances when $Plk4^{\Delta u/\Delta u}$ animals did produce pups, the litter size was small, averaging approximately four to five pups. The fertility of $Plk4^{\Delta u/\Delta u}$ females was poor throughout their lives, while male $Plk4^{\Delta u/\Delta u}$ animals showed improved fecundity with increasing age (Supplemental Fig. S3A,B).

Consistent with the strong reduction in fertility, $Plk4^{\Delta u/\Delta u}$ males produced ~10-fold less sperm than littermate control animals at 8–12 wk of age (Fig. 3C). The residual sperm generated by $Plk4^{\Delta u/\Delta u}$ males had a normal flagellum length and a swimming velocity similar to that of $Plk4^{+/+}$ and $Plk4^{+/\Delta u}$ animals (Supplemental Fig. S3C, D). To determine why $Plk4^{\Delta u/\Delta u}$ males generate fewer sperm, we analyzed the testes of animals at the beginning of spermatogenesis (P27–P28) (Fig. 3D). Only 17% of the seminiferous tubules of $Plk4^{\Delta u/\Delta u}$ testes contained $SYCP3^+$ meiotic cells, compared with 90%–94% of tubules in $Plk4^{+/+}$ and $Plk4^{+/\Delta u}$ animals (Fig. 3E,F). The testes of $Plk4^{\Delta u/\Delta u}$ mice also showed a severe reduction in $SYCP3^-$ $DAZL^+$ premeiotic germ cells and showed no enrichment for meiotically arrested cells (Fig. 3E–G). Furthermore, testes from neonatal (P0) $Plk4^{\Delta u/\Delta u}$ mice already displayed a severe depletion of $DAZL^+$ tubules (Fig. 3H,I), indicating that the gametogenesis defects in $Plk4^{\Delta u/\Delta u}$ males arise prior to meiotic entry.

Female oocytes enter meiosis during embryonic development and remain arrested in prophase I as primordial follicles (Supplemental Fig. S3E). During each estrous cycle, groups of primordial follicles mature and progress through meiosis and arrest at metaphase II until fertilized. Analysis of female $Plk4^{\Delta u/\Delta u}$ ovaries revealed a decreased density of oocyte follicles and a lower fraction of primordial follicles at P15 and P30, a sign of premature attrition of germ cells (Supplemental Fig. S3F–K). Taken together, these observations suggest that the fertility defects in $Plk4^{\Delta u/\Delta u}$ mice are caused by a depletion of premeiotic germ cells.

Plk4 *uORFs prevent centriole amplification in primordial germ cells*

Male and female germ cells originate from ~40 primordial germ cells (PGCs) that are specified around embryonic day 6.5 (E6.5) (Saitou and Yamaji 2012). Between E7.5 and E10.5, PGCs migrate and colonize the developing gonads (Fig. 4A). To test whether loss of *Plk4* uORFs resulted in defects in PGC development, we examined PGCs between E10.25 and E10.5, when they first arrive at the genital ridges. Analysis of embryos at E10.25 revealed a similar localization of migrating $OCT4^+$ PGCs within the dorsal mesentery in littermate $Plk4^{+/+}$, $Plk4^{+/\Delta u}$, and $Plk4^{\Delta u/\Delta u}$ animals (Fig. 4B). This suggests that PGCs from $Plk4^{\Delta u/\Delta u}$ mice follow a normal migratory route to reach the gonads. At E10.5, when PGCs have completed migration, the presence of $OCT4^+$ PGCs that reached the genital ridges also appeared similar across all genotypes (Fig. 4B). Nevertheless, a small fraction of $Plk4^{\Delta u/\Delta u}$ PGCs at E10.5 had an increased number of centrin-GFP foci that were often observed in a "flower-like" pattern (Fig. 4C,D). These rosettes of extra centrin foci are reminiscent of what is

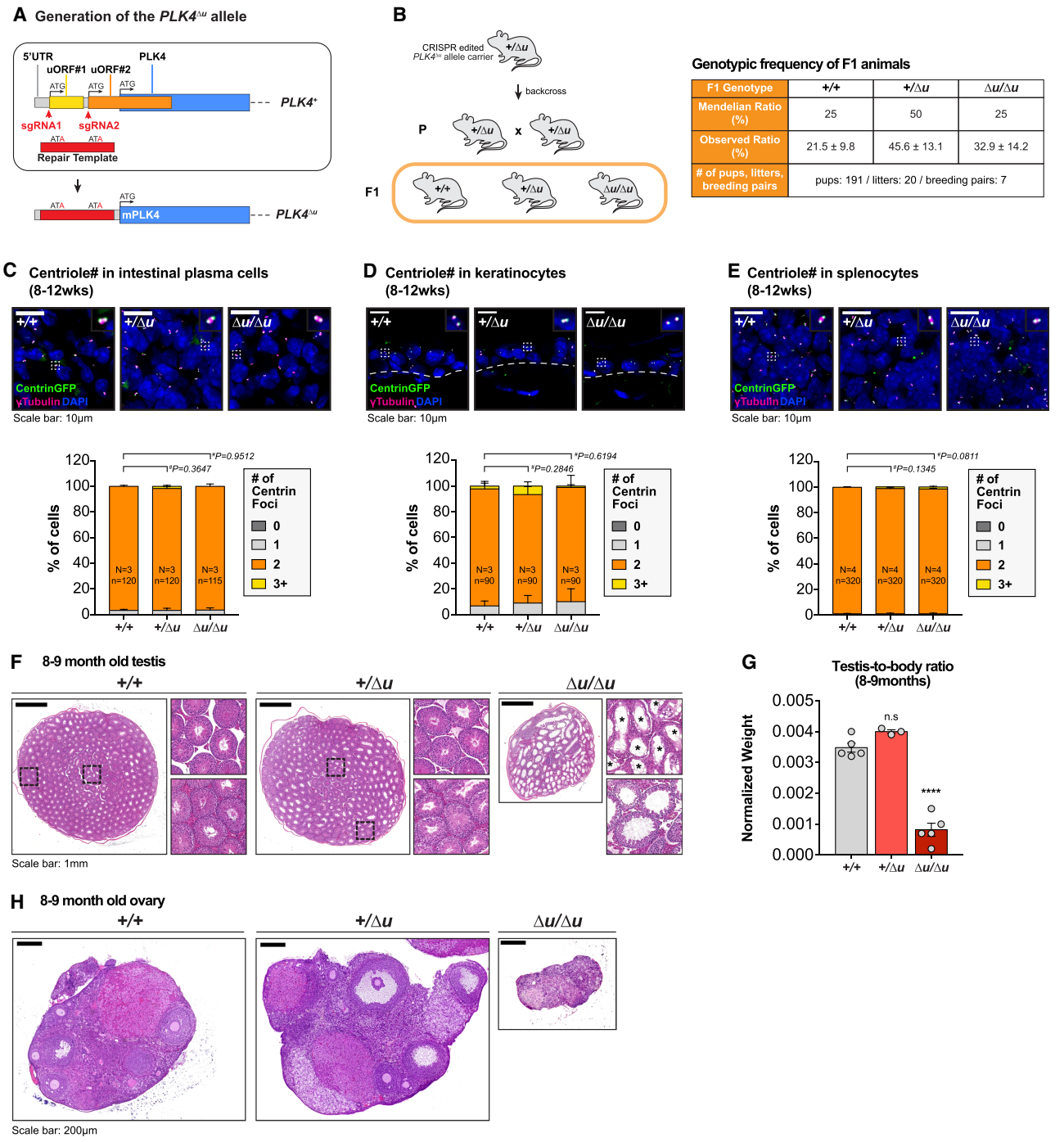

Figure 2. Mice lacking *Plk4* uORFs display reduced fertility. (*A*) Diagram showing the strategy used to generate the $Plk4^{\Delta u}$ allele in mice using CRISPR/Cas9. sgRNAs that cut within the proximity of the uORF1 and uORF2 start codons were coinjected with a ssDNA repair template. (*B*, *left*) Scheme showing the breeding strategy used to generate the F1 genotypes. (*Right*) Table showing the expected and observed ratios of F1 mice with the indicated genotypes. (*C–E*, *top*) Representative immunofluorescent images of intestinal plasma cells (*C*), keratinocytes (*D*), and splenocytes (*E*) from 8- to 12-wk-old $Plk4^{+/+}$, $Plk4^{+/\Delta u}$, and $Plk4^{\Delta u/\Delta u}$ mice. Cells expressing centrin-GFP (green) were stained with antibodies against γ-tubulin (magenta) and DAPI (blue). *Insets* show zoomed-in views of representative centrosome foci. Scale bar, 10 μm. (*Bottom*) Quantification of the number of centrin foci in the indicated genotypes. $N \geq 3$ mice, $n \geq 90$ cells. (#) χ^2 test, (*) post-hoc analysis. (*F*) Representative histology images of testis tissue from 8- to 9-mo-old mice with the indicated genotypes. *Insets* show zoomed-in views of two representative tissue regions; asterisks indicate empty seminiferous tubules lacking spermatozoa. Scale bar, 1 mm. (*G*) Quantification of the testis to body weight ratio in 8- to 9-mo-old male mice with the indicated genotypes. $N \geq 3$ mice; one-way ANOVA with post-hoc analysis. (*H*) Representative histology images of ovary tissue from 8- to 9-mo-old mice with the indicated genotypes. Scale bar, 200 μm. All data represent the means ± SEM. (****) $P < 0.0001$, (n.s) not significant ($P > 0.05$). (*N*) Number of biological replicates/mice, (*n*) number of cells analyzed.

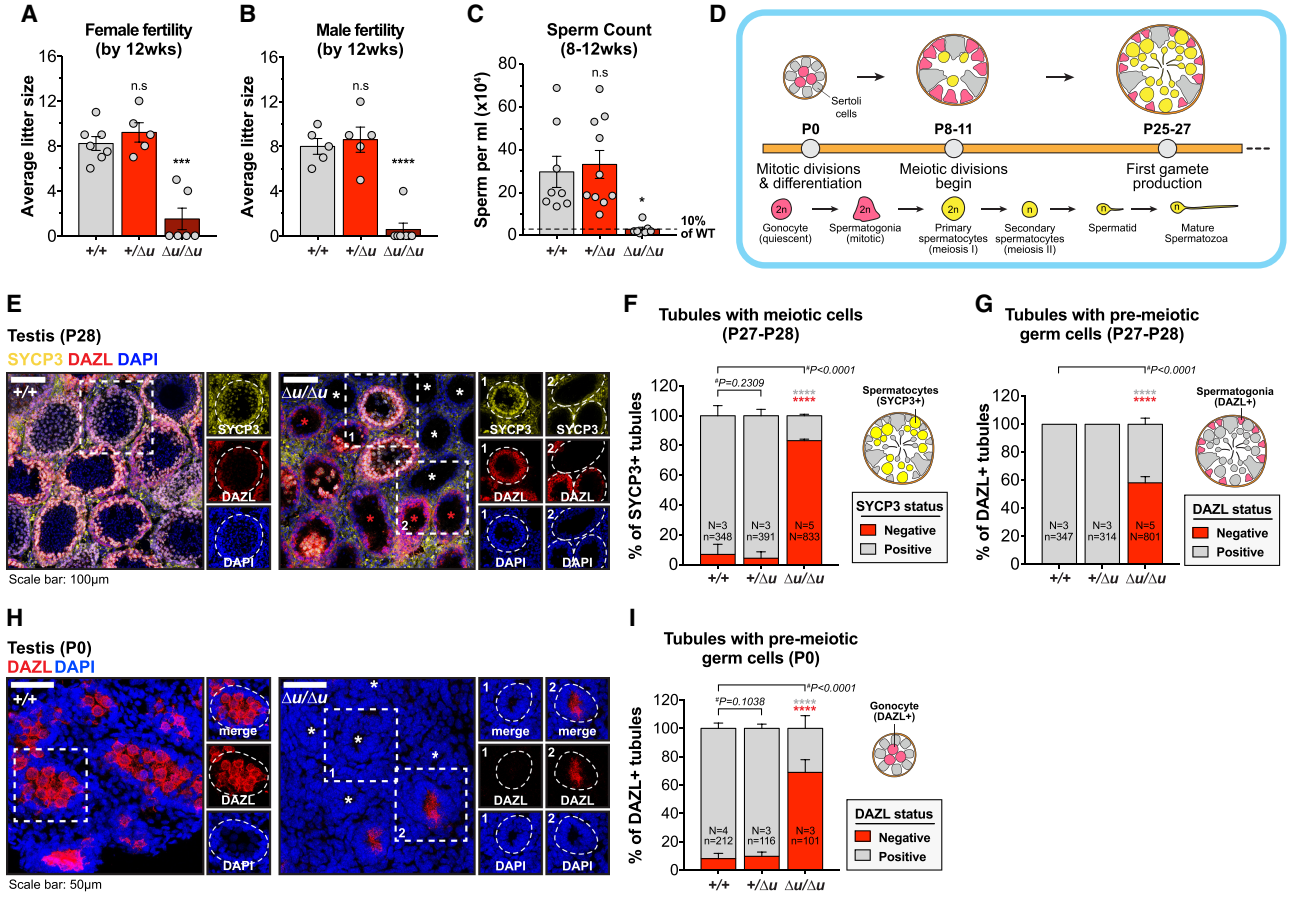

Figure 3. Loss of *Plk4* uORFs leads to premeiotic germ cell depletion. (*A*,*B*) Graph showing average litter size produced by 12-wk-old female (*A*) and male (*B*) mice. $N \geq 5$ mice; one-way ANOVA with post-hoc analysis. (*C*) Graph showing sperm count from the isolated epididymis of 8- to 12-wk-old male mice with the indicated genotypes. The black dashed line represents 10% of the Plk4$^{+/+}$ average sperm concentration, the level below which mice are considered infertile. $N \geq 7$ mice; one-way ANOVA with post-hoc analysis. (*D*) Diagram of postnatal testis and sperm development in mice. Cross-section of a single tubule is shown with Sertoli cells in gray and germ cells at different developmental stages. At P0, quiescent gonocytes, the precursors of male gametes, resume proliferation and differentiate into spermatogonia. Starting at P8–P11, spermatogonia begin to enter meiosis, forming primary and secondary spermatocytes. The first spermatozoa with elongated flagellum start to appear around P25–P27. (*E*) Representative immunofluorescent images of testis tissue sections from P28 male mice with the indicated genotypes. Tissue was stained with antibodies against the meiotic marker SYCP3 (yellow), spermatogonia marker DAZL (red), and DAPI (blue). White asterisks indicate tubules lacking germ cells, and red asterisks indicate tubules with DAZL^{+} germ cells but lacking SYCP3^{+} meiotic cells. *Insets* show zoomed-in views of representative seminiferous tubules. Scale bar, 100 μm. (*F*,*G*) Percentage of tubules containing SYCP3^{+} meiotic (*F*) or SYCP3^{-} DAZL^{+} premeiotic (*G*) germ cells from P27–P28 male mice with the indicated genotypes. $N \geq 3$ mice, $n \geq 314$ tubules. (#) χ^2 test, (*) post-hoc analysis. (*H*) Representative immunofluorescent images of testis tissue sections from P0 male mice with the indicated genotypes. Tissue was stained with antibodies against spermatogonia marker DAZL (red) and DAPI (blue). White asterisks indicate tubules lacking germ cells. *Insets* show zoomed-in views of representative seminiferous tubules. Scale bar, 50 μm. (*I*) Percentage of tubules containing gonocytes from P0 male mice with the indicated genotypes. $N \geq 3$ mice, $n \geq 101$ tubules. (#) χ^2 test, (*) post-hoc analysis. All data represent the means ± SEM. (*) $P < 0.05$, (***) $P < 0.001$, (****) $P < 0.0001$, (n.s) not significant ($P > 0.05$). (*N*) Number of biological replicates/mice, (*n*) number of seminiferous tubules analyzed.

frequently observed in cells following PLK4 overexpression, where multiple procentrioles form around the base of a pre-existing parent centriole in S phase.

Starting from E10.5, PGCs begin to proliferate rapidly, increasing from ~500 cells to ~25,000 cells by E13.5 (Tam and Snow 1981; Laird et al. 2011). To investigate whether the loss of PLK4 uORFs has an impact on this rapid proliferation, we stained E13.5 embryos for the PGC marker DDX4. *Plk4*$^{\Delta u/\Delta u}$ animals displayed an approximately fivefold and ~sevenfold reduction in PGC density in the developing gonads of male and female embryos, respectively (Fig. 4E,F). The surviving PGCs in *Plk4*$^{\Delta u/\Delta u}$ animals had an increased number of centrin-GFP foci associated with the PCM protein γ-tubulin (Fig. 4G,H; Supplemental Fig. S4A). Expansion microscopy on *Plk4*$^{\Delta u/\Delta u}$ tissue sections confirmed that the extra centrin foci represented bona fide centriole amplification (Supplemental Fig. S4B,C). Importantly, supernumerary centrioles were only found in PGCs and not in surrounding (DDX4^{-}) cells of the gonad (Fig. 4I).

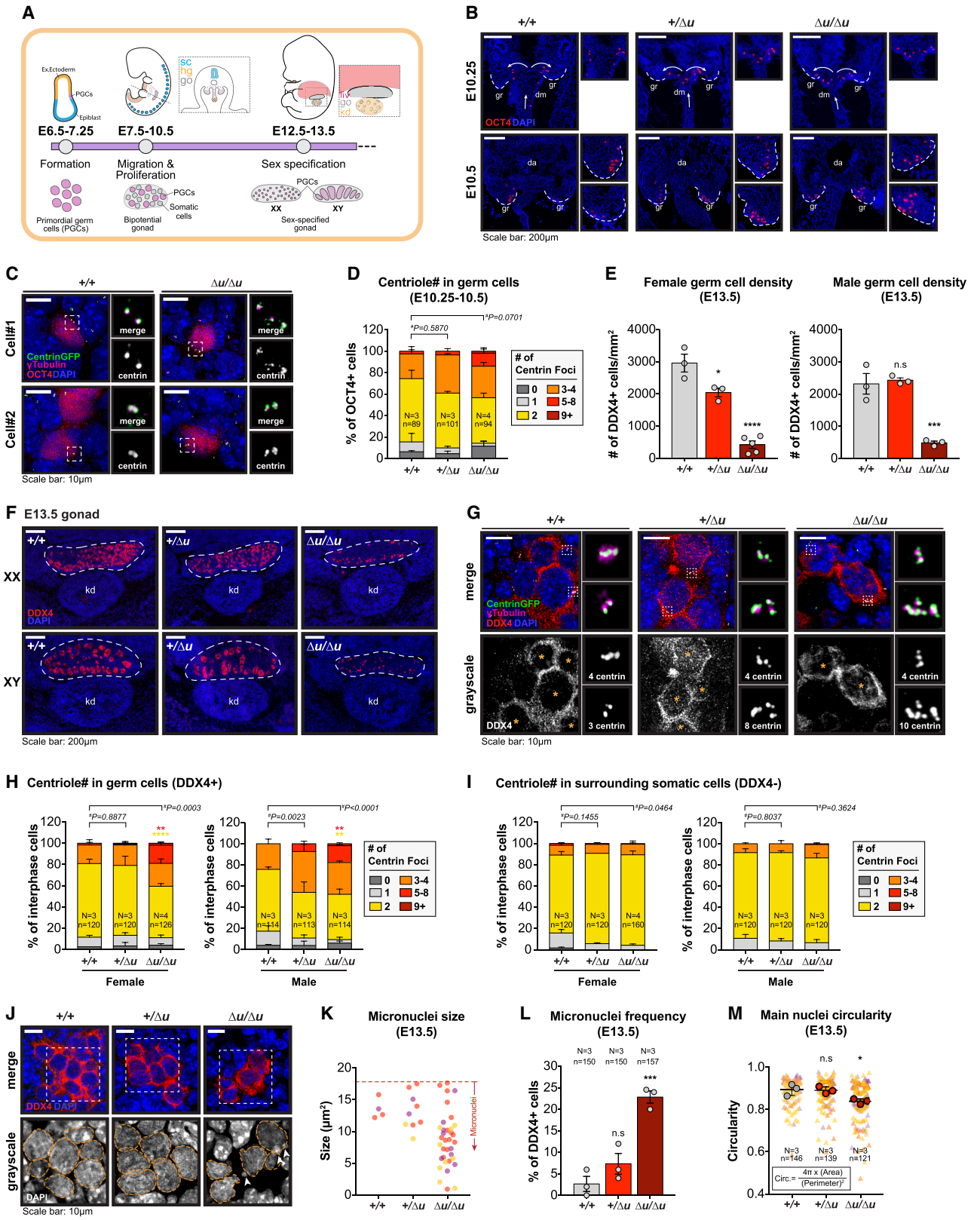

Figure 4. *See legend on following page.*

Some $Plk4^{\Delta u/\Delta u}$ PGCs with supernumerary centrioles exhibited multipolar mitotic spindles, suggesting that these cells could generate aneuploid daughter cells with micronuclei or abnormal nuclear shape (Supplemental Fig. S4D). To determine whether centriole amplification in $Plk4^{\Delta u/\Delta u}$ PGCs indeed led to mitotic errors, we analyzed the size and shape of nuclei in E13.5 PGCs. A micronucleus was defined as a nucleus with an area smaller than two standard deviations below the mean of $Plk4^{+/+}$ PGCs (<17.8 μm^2) (Supplemental Fig. S4E). The frequency of micronuclei was increased by ~10-fold in E13.5 $Plk4^{\Delta u/\Delta u}$ PGCs compared with wild-type controls (Fig. 4J–L). Moreover, the majority of $Plk4^{\Delta u/\Delta u}$ PGC nuclei were often irregular in shape and showed a decreased circularity index (Fig. 4M). These results indicate that centriole amplification in $Plk4^{\Delta u/\Delta u}$ PGCs results in extensive chromosome segregation errors that may be responsible for cell death and depletion of the PGC pool.

PGC depletion in $Plk4^{\Delta u/\Delta u}$ *mice is caused by the overproduction of PLK4*

PGC development is associated with a remarkable level of epigenetic reprogramming that results in significant changes in their transcriptional output (Lee et al. 2002; Seki et al. 2005, 2007; Hajkova et al. 2008; Saitou et al. 2012). A previous study analyzing the mouse PGC transcriptome revealed that on a per-cell basis, PGCs produce threefold to fourfold more mRNA than neighboring somatic cells (Percharde et al. 2017). *Plk4* is among the transcripts that are highly up-regulated (eightfold to 11-fold increase or 3–3.5 $\log_2$ fold change) during this period of hypertranscription in PGCs (Supplemental Fig. S5A). Consistent with this report, we observed a higher *Plk4* mRNA copy number in dissociated PGCs compared with surrounding somatic cells using single-molecule fluorescence in situ hybridization (Supplemental Fig. S5B,C). This led us to hypothesize that PGCs may be more sensitive to an increase in PLK4 translation because of the elevated abundance of the *Plk4* mRNA. Thus, we reasoned that reducing the level of *Plk4* transcripts in mice that lack uORFs would rescue the fertility defects observed in $Plk4^{\Delta u/\Delta u}$ animals. To test this idea, we reduced *Plk4* transcript levels by generating compound heterozygous animals carrying a $Plk4^{\Delta u}$ allele and a *Plk4*-null allele (referred to here as $Plk4^{\Delta u/-}$ mice) (Fig. 5A). As expected, $Plk4^{\Delta u/-}$ mouse embryonic fibroblasts (MEFs) had an ~50% reduction in *Plk4* mRNA levels compared with $Plk4^{\Delta u/\Delta u}$ cells (Fig. 5B). Moreover, sequencing of the 5′ UTR of the *Plk4* cDNA confirmed that $Plk4^{\Delta u/-}$ MEFs did not contain detectable levels of mRNA encoding wild-type uORF1 and uORF2, indicating that the frameshifted mRNA produced by the *Plk4*-null allele undergoes efficient nonsense-mediated decay (Fig. 5C).

The majority of $Plk4^{\Delta u/-}$ males and females generated litters of a size comparable with those of $Plk4^{+/+}$ animals (Fig. 5D,E). This restoration of fertility was accompanied

Figure 4. $Plk4^{\Delta u/\Delta u}$ mice have reduced numbers of primordial germ cells. (*A*) Diagram showing the development of germ cells during embryonic development in mice. Key events include the formation of PGCs at approximately E6.5, their proliferation and migration through the hindgut to the genital ridge between E7.5 and E10.5, and colonization of the developing gonad between E10.5 and E13.5. Sex specification begins around E11.5 and is complete by E13.5. Zoomed-in cross-sections of the gonads are included to show the relative position of the gonad compared with other developing organs. (go) Gonad, (sc) spinal cord, (hg) hindgut, (liv) liver, (kd) kidney. (*B*) Representative immunofluorescent images of gonad tissue sections from E10.25 (*top*) and E10.5 (*bottom*) $Plk4^{+/+}$, $Plk4^{+/\Delta u}$, and $Plk4^{\Delta u/\Delta u}$ embryos. Tissues were stained with antibodies for OCT4 (red) and DAPI (blue). The white dashed line shows the outline of the genital ridge (gr), and white arrows show the direction of migrating PGCs along the dorsal mesentery (dm). *Insets* show zoomed-in views of the dorsal mesentery at E10.25 (*top*) and each genital ridge at E10.5 (*bottom*). Scale bar, 200 µm. (*C*) Representative immunofluorescent images of centrioles from E10.5 PGCs with the indicated genotypes. Cells expressing centrin-GFP (green) were stained with antibodies against γ-tubulin (magenta), OCT4 (red), and DAPI (blue). *Insets* show zoomed-in views of representative centrosome foci. Scale bar, 10 µm. (*D*) Quantification of the number of centrin foci in $OCT4^+$ PGCs from E10.25–E10.5 embryo gonads of the indicated genotypes. $N \geq 3$ mice, $n \geq 89$ cells. (#) χ^2 test, (*) post-hoc analysis. (*E*) Quantification of PGC density in the gonads of E13.5 female and male embryos with the indicated genotypes. $N \geq 3$ mice; one-way ANOVA with post-hoc analysis. (*F*) Representative immunofluorescent images of gonad tissue sections from E13.5 female (XX) and male (XY) $Plk4^{+/+}$, $Plk4^{+/\Delta u}$, and $Plk4^{\Delta u/\Delta u}$ embryos. Tissues were stained with antibodies for DDX4 (red) and DAPI (blue). The white dashed line shows the outline of the gonad. (kd) Kidney. Scale bar, 200 µm. (*G*) Representative immunofluorescent images of centrioles in PGCs from E13.5 gonads from male embryos with the indicated genotypes. Cells expressing centrin-GFP (green) were stained with antibodies against γ-tubulin (magenta), DDX4 (red), and DAPI (blue). *Insets* show zoomed-in views of representative centrosome foci. Scale bar, 10 µm. (*H*,*I*) Quantification of the number of centrin foci in $DDX4^+$ PGCs (*H*) and surrounding somatic cells (*I*) from E13.5 female and embryo gonads of the indicated genotypes. $N \geq 3$ mice, $n \geq 113$ cells. (#) χ^2 test, (*) post-hoc analysis. (*J*) Representative immunofluorescent images of cell nuclei from E13.5 male gonads with the indicated genotypes. Tissues were stained with antibodies for DDX4 (red) and DAPI (blue). *Insets* show zoomed-in views of nuclei from representative $DDX4^+$ PGCs. The orange dashed line shows the outline of PGC nuclei, and the white arrowhead indicates the presence of micronuclei. Scale bar, 10 µm. (*K*) Graph showing the distribution of nucleus size of E13.5 PGCs from male embryos of the indicated genotypes. The red dashed line indicates the cutoff for micronuclei (nuclei that are two SD below the average nuclei measured in $Plk4^{+/+}$). $N \geq 3$ mice, $n \geq 150$ cells. (*L*) Quantification of micronucleus frequency among $DDX4^+$ PGCs in E13.5 male gonads of embryos of the indicated genotypes. $N = 3$ mice, $n \geq 150$ cells; one-way ANOVA with post-hoc analysis. (*M*) Quantification of the circularity of the main nuclei of $DDX4^+$ PGCs in E13.5 male gonads from embryos of the indicated genotypes. Circularity was determined by the formula shown. Triangles represent individual cells, triangles of the same color represent cells from the same embryo, and circles represent the average circularity of cells from each embryo. $N = 3$ mice, $n \geq 121$ cells; one-way ANOVA with post-hoc analysis. All data represent the means ± SEM. (*) $P < 0.05$, (**) $P < 0.01$, (***) $P < 0.001$, (****) $P < 0.0001$, (n.s) not significant ($P > 0.05$). (*N*) Number of biological replicates/mice, (*n*) number of cells analyzed.

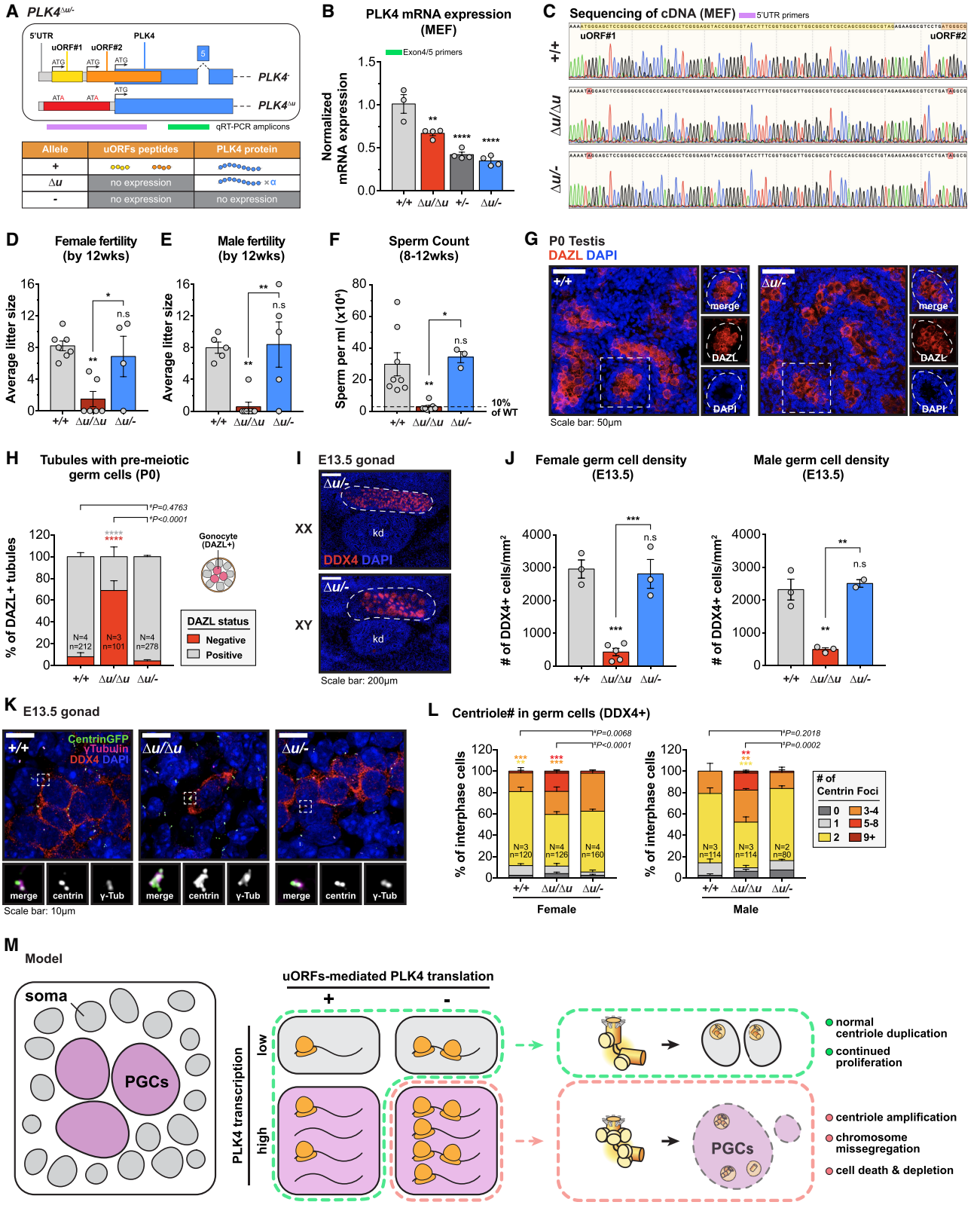

Figure 5. *See legend on following page.*

by normal seminiferous tubule development and sperm production in 8- to 12-wk-old *Plk4*$^{\Delta u/-}$ males (Fig. 5F; Supplemental Fig. S5D,E), as well as rescued germ cell number at P0 (Fig. 5G,H). Finally, both male and female *Plk4*$^{\Delta u/-}$ animals had normal numbers of PGCs present in the developing gonad at E13.5 (Fig. 5I,J). In addition, *Plk4*$^{\Delta u/-}$ PGCs no longer display centriole amplification (Fig. 5K,L). Collectively, these results suggest that reducing the level of *Plk4* mRNA restores normal centriole number by counterbalancing the increase in PLK4 translation in PGCs following the loss of uORFs.

Discussion

PLK4 is a dosage-sensitive kinase whose levels must be carefully controlled to maintain centriole number in proliferating cells (Bettencourt-Dias et al. 2005; Habedanck et al. 2005). Excess PLK4 leads to the formation of extra centrioles and increases the frequency of chromosome segregation errors during cell division (Ganem et al. 2009; Silkworth et al. 2009). To protect against genome instability, cells maintain PLK4 protein levels through a strict negative feedback loop in which the active kinase targets itself for degradation by the proteasome (Cunha-Ferreira et al. 2009, 2013; Rogers et al. 2009; Guderian et al. 2010; Holland et al. 2010, 2012; Klebba et al. 2013). Here, we discovered that translational suppression by uORFs provides an additional pathway to down-regulate the production of PLK4 protein (Fig. 5M). We show that uORF1 suppresses translation of uORF2, thereby enabling translational reinitiation to occur, with a reduced probability, at the downstream ATG of *PLK4*. Meanwhile, uORF2 likely acts as a buffer to sequester ribosomes that fail to initiate translation at uORF1. uORF1 has a strong and highly conserved translational initiation context, and blocking ribosome elongation leads to the accumulation of ribosomes at the ATG of uORF1 (Fig. 1A; Supplemental Fig. S1A). This suggests the uORF1 is the central mediator of PLK4 translational suppression, while uORF2 has a minor role in improving the robustness of the system. Consistent with this interpretation, uORF1 is present in the *PLK4* mRNAs of all vertebrates analyzed, while the presence of uORF2 is much less conserved. Furthermore, mice lacking only uORF2 (*Plk4*$^{u1/u1}$) have no observable defects (Supplemental Fig. S5F,G). Thus, we propose that the production of PLK4 occurs primarily through translation reinitiation downstream from uORF1.

Removal of both PLK4 uORFs was well tolerated in *Plk4*$^{\Delta u/\Delta u}$ mice and did not lead to global PLK4 overexpression or centriole amplification. However, mice that lacked PLK4 uORFs had dramatically reduced fertility that was caused by a depletion of PGCs. PGCs lacking uORFs displayed centriole amplification, evidence of micronucleation, and abnormal nuclear architecture. This suggests that the overproduction of PLK4 in PGCs promotes centriole amplification and cell division errors that drive cell death. Mammalian PGC development normally relies on programmed cell death to remove abnormal, misplaced, or excess cells (Wang et al. 1998; Runyan et al. 2006; Aitken et al. 2011; Nguyen et al. 2020). The elevated sensitivity of PGCs to cell death cues may explain why they are readily eliminated following cell division errors.

Although uORFs have been shown to regulate the expression of genes in response to specific environmental conditions, to our knowledge, our study is among the few to demonstrate that the loss of uORF-mediated protein expression can lead to a cell type-specific defect. A central

Figure 5. Reducing the expression of *Plk4* rescues the fertility defect in mice lacking *Plk4* uORFs. (*A*) Diagram showing the two genetic alleles of a *Plk4*$^{\Delta u/-}$ mouse model. The *Plk4*$^{-}$ allele lacks exon 5, generating a frameshifted protein that undergoes premature translational termination. (*B*) Graph showing *Plk4* mRNA abundance in MEF cells as measured by qRT-PCR. $N = 4$, each with technical triplicate; one-way ANOVA with post-hoc analysis. (*C*) Sequencing trace from *Plk4* cDNA of MEF cells of the indicated genotypes. (*D*,*E*) Graph showing average litter size produced by 12-wk-old female (*D*) and male (*E*) *Plk4*$^{\Delta u/-}$ mice. $N \geq 5$ mice; one-way ANOVA with post-hoc analysis. *Plk4*$^{+/+}$ and *Plk4*$^{\Delta u/\Delta u}$ data are from Figure 3, A and B, and are shown alongside for comparison. (*F*) Graph showing sperm count from isolated epididymis of 8- to 12-wk-old *Plk4*$^{\Delta u/-}$ male mice. The black dashed line indicates 10% of the *Plk4*$^{+/+}$ average sperm concentration. $N = 3$ mice; one-way ANOVA with post-hoc analysis. *Plk4*$^{+/+}$ and *Plk4*$^{\Delta u/\Delta u}$ data are from Figure 3C and are shown alongside for comparison. (*G*) Representative immunofluorescent images of testis tissue sections from P0 *Plk4*$^{+/+}$ and *Plk4*$^{\Delta u/-}$ male mice. Tissues were stained with antibodies against the spermatogonia marker DAZL (red) and DAPI (blue). *Insets* show zoomed-in views of representative seminiferous tubules. Scale bar, 50 µm. (*H*) Percentage of tubules containing gonocytes from P0 *Plk4*$^{\Delta u/-}$ male mice. $N = 4$ mice, $n = 278$ tubules. (#) χ^2 test, (*) post-hoc analysis. *Plk4*$^{+/+}$ and *Plk4*$^{\Delta u/\Delta u}$ are from Figure 3I and are shown alongside for comparison. (*I*) Representative immunofluorescent images of gonad tissue sections from E13.5 female (XX) and male (XY) mice of the indicated genotypes. Tissues were stained with antibodies for DDX4 (red) and DAPI (blue). The white dashed line shows the outline of the gonad. (kd) Kidney. Scale bar, 200 µm. (*J*) Quantification of PGC density in the gonads of E13.5 *Plk4*$^{\Delta u/-}$ female and male mice. $N \geq 2$ mice; one-way ANOVA with post-hoc analysis. *Plk4*$^{+/+}$ and *Plk4*$^{\Delta u/\Delta u}$ data are from Figure 4E and are shown alongside for comparison. (*K*) Representative immunofluorescent images of centrioles in PGCs from E13.5 gonads from male mice of the indicated genotypes. Cells expressing centrin-GFP (green) were stained with antibodies against γ-tubulin (magenta), DDX4 (red), and DAPI (blue). *Insets* show zoomed-in views of representative centrosome foci. Scale bar, 10 µm. (*L*) Quantification of the number of centrin foci in DDX4^{+} PGCs from E13.5 *Plk4*$^{\Delta u/-}$ gonads from female and male mice. $N = 2$ mice, $n = 80$ cells. (#) χ^2 test, (*) post-hoc analysis. *Plk4*$^{+/+}$ and *Plk4*$^{\Delta u/\Delta u}$ data are from Figure 4H and are shown alongside for comparison. (*M*) Model for regulation of PLK4 abundance in PGCs versus somatic cells. During normal development, PGCs undergo hypertranscription and produce ~10-fold more *Plk4* transcripts than somatic cells. uORFs act as translational suppressors that counterbalance the high transcript levels to limit PLK4 production. In the absence of uORFs, translation is derepressed, allowing extra PLK4 to accumulate. This leads to centriole amplification, chromosome missegregation, and the eventual depletion of PGCs. All data represent the means ± SEM. (*) $P < 0.05$, (**) $P < 0.01$, (***) $P < 0.001$, (****) $P < 0.0001$, (n.s) not significant ($P > 0.05$). (*N*) Number of biological replicates/mice, (*n*) number of cells analyzed.

question that emerges from our study is why the loss of PLK4 uORFs appears to uniquely drive PLK4 overexpression and centriole amplification in PGCs. One possibility is that PGCs express higher levels of *Plk4* transcript than other cell types and thus produce more PLK4 protein when translation is increased following the loss of uORFs. Indeed, previous work comparing the transcriptome of PGCs with the surrounding soma revealed that many transcripts, including *Plk4*, are hypertranscribed in PGCs (Percharde et al. 2017). According to this study, *Plk4* mRNA levels are eightfold to 11-fold higher in PGCs at E13.5. This increase in Plk4 transcripts may be sufficient, in the absence of uORFs, to surpass a threshold level of PLK4 that promotes centriole amplification. Consistently, we show that an ~50% reduction in the level of *Plk4* mRNA was sufficient to restore normal centriole copy number and rescue PGC proliferation in $Plk4^{\Delta u/-}$ animals. Importantly, this occurred without the restored expression of the uORF-encoded peptides. In addition, $Plk4^{+/\Delta u}$ mice with only one $Plk4^{\Delta u}$ allele are fertile, while homozygous $Plk4^{\Delta u/\Delta u}$ mice have dramatically reduced fertility (Fig. 3A, B; Supplemental Fig. S3A,B). This indicates that PLK4 levels must increase past a specific level to significantly deplete PGCs and elicit an organismal phenotype. Together, these results suggest that the unique transcriptional profile of PGCs renders them highly dependent on uORFs to suppress *Plk4* translation and prevent centriole amplification.

Despite the broad expression of PLK4 across many cell types in vivo, some mutations in PLK4 have been reported to specifically impact mammalian gametogenesis. A heterozygous deletion in *PLK4* that introduces a premature stop codon in the kinase domain has been linked to azoospermia and infertility in humans (Miyamoto et al. 2016). Meanwhile, a heterozygous point mutation in the kinase domain of *Plk4* leads to reduced testis size, germ cell loss, and subfertility in mice (Harris et al. 2011). Previous studies have reported a similar germ cell-specific sensitivity to mutations in other mitotic regulators, including separase and KIF18A (Reinholdt et al. 2006; Xu et al. 2011; Czechanski et al. 2015). Mice homozygous for the *Kif18a* mutation germ cell depletion 2 (gcd2) have defects in chromosome alignment and elevated levels of micronuclei across multiple somatic tissues (Sepaniac et al. 2021). However, while $Kif18a^{gcd2/gcd2}$ cells in somatic tissues progress through mitosis and remain healthy, germ cells with similar chromosome misalignment phenotypes undergo mitotic arrest and apoptosis, leading to sterility (Czechanski et al. 2015). This suggests that PGCs have a low tolerance for mitotic errors or mitotic delays, likely because chromosome segregation errors in the germline have a direct consequence on organism fitness across generations. Thus, in addition to being more susceptible to overproducing PLK4 due to hypertranscription, PGCs may also be more sensitive to the consequence of its overexpression.

In conclusion, we have identified uORFs as conserved elements for controlling the abundance of PLK4. While this mode of regulation is dispensable in most cell types in vivo, it has a uniquely important contribution in PGCs. By suppressing translation, uORFs help counter the effect of PLK4 hypertranscription in PGCs, thereby preventing centriole amplification and maintaining the genetic integrity of future gametes. This may explain why *PLK4* uORFs have remained positively selected for throughout vertebrate evolution.

Materials and methods

Cloning

All PLK4 reporter constructs were cloned into a pcDNA5/FRT/TO vector backbone (Life Technologies) and expressed from a CMV promoter under the control of two tetracycline operator sites. The detailed configuration of each is indicated in the figure and figure legend for each experiment. The ecDHFR-sfGFP-NLS cassette was subcloned from a plasmid purchased from Addgene (67929).

Cell culture and drug treatments

Generation of primary MEF cultures MEFs were harvested as previously described (Xu 2005). Briefly, embryos were harvested at E12.5–E14.5 and incubated in 0.05% trypsin-EDTA (Thermo Scientific) overnight at 4°C. The following day, the embryos were incubated for 5 min at 37°C and cells were dissociated by pipetting.

Generation of stable Dox-inducible reporter cell lines Flp-In TRex-DLD-1 cells (a gift from S. Taylor, University of Manchester, Manchester, UK) were engineered using the Flp-In TRex core kit (Life Technologies) to stably express the tetracycline repressor protein and contain a single, genomic Flp recombination target site (FRT)/lacZeo site. Stable, isogenic cell lines expressing variations of the PLK4 reporter were generated by cotransfecting the pcDNA5 construct and pOG44 FLP recombinase vector using X-tremeGENE HP DNA transfection reagent (Millipore Sigma). Expression of all reporters was induced with 1 µg/mL doxycycline (Millipore Sigma) unless indicated otherwise.

Culture conditions DLD-1 cells were grown in DMEM medium (Cellgro, Corning) containing 100 U/mL penicillin, 100 U/mL streptomycin, 2 mM L-glutamine, and 10% fetal bovine essence (Seradigm). Cells were maintained at 37°C in a 5% CO_2 atmosphere with 21% O_2.

Mouse embryonic fibroblasts (MEFs) were grown in DMEM (Cellgro, Corning) supplemented with 10% fetal bovine serum (Sigma), 100 U/mL penicillin/100 U/mL streptomycin, and 0.1 mM β-mercaptoethanol. Cells were maintained at 37°C in a 5% CO_2 atmosphere with 3% O_2.

Flow cytometry

Evaluation of EGFP expression in reporter cell lines was performed using the Guava EasyCyte flow cytometer. Briefly, cells were trypsinized, washed, and resuspended in PBS for analysis. Data from 10,000 cells were acquired for each sample. All fluorescent intensity measurements were normalized to the signal from a nonfluorescent control.

Immunofluorescence staining in cultured cells

Cells were grown on glass coverslips and fixed for 8 min in ice-cold MeOH at −20°C. Cells were blocked in blocking solution (2.5% FBS, 200 mM glycine, 0.1% Triton X-100 in PBS) for 1 h

at room temperature or overnight at 4°C. Cells were then incubated in primary antibody diluted in the blocking solution for 1 h and rinsed with PBST (0.1% Triton X-100 in PBS), followed by secondary antibody staining prepared in the same blocking solution. DNA was stained with DAPI, and cells were mounted in ProLong Gold antifade mountant (Invitrogen). The following primary antibodies were used: rabbit centrin (1:1000; in-house, raised against human centrin2 [amino acids 1–172]) and goat CEP192 (1:1000; in-house, raised against CEP192 [amino acids 1–211]). Both primary antibodies were directly conjugated to Alexa fluor 488, 555, or 647 (Thermo Fisher Scientific). Details on antibodies are also listed in Supplemental Table S1.

Immunofluorescence images were acquired at room temperature (25°C) using a DeltaVision Elite system (GE Healthcare) controlling a scientific CMOS camera (pco.edge 5.5). Images were acquired using an Olympus 40×, 1.35 NA oil objective with Applied Precision immersion oil ($n = 1.516$) at 40× with 0.2-µm z-sections. Acquisition parameters were controlled by SoftWoRx suite (GE Healthcare).

Live-cell microscopy

A monoclonal iRFP-tagged PCNA Flp-In TRex-DLD-1 cell line was used to stably express the truncated PLK4-sfGFP-NLS reporters. Cells expressing either a uORF1+2 or a uORFs mut version of the reporter were seeded into four-chamber, 35-mm glass-bottom culture dishes (Greiner) along with 1 µg/mL doxycycline 1 d before starting the time-lapse imaging. The next day, cells were transferred to an environmental control station set to 37°C and 5% CO_2. Time-lapse movies were captured using a SP8 microscope (Leica microsystems) controlling a Leica DFC9000 GTC sCMOS camera. Images were acquired with a 40×, 1.30 NA oil objective. Every 5 min, six 3-µm z-sections were acquired in the GFP and far-red channels to observe the sfGFP-NLS and iRFP-PCNA signals, respectively. Images were acquired using Leica type F immersion oil ($n = 1.5180$). Approximately 3–4 h into the movie, prewarmed media containing either DMSO or TMP (to 50 µM final concentration) was carefully added to each imaging chamber.

The translation rates of uORF1+2 and uORFs mut reporters were calculated by normalizing the fluorescence intensity of nuclear-localized sfGFP in TMP-treated cells to the DMSO condition at the same time point. An additional normalization was performed to the average signal intensity from the imaging frame prior to DMSO or TMP addition.

Animals

Plk4$^{\Delta u/\Delta u}$ mice were generated using CRISPR/Cas9. Two sgRNAs (uORF1 sgRNA [5′-CCGGCGGGAATTTTTCAAAA-3′] and uORF2 sgRNA [5′-GCGTAGAGAAGGCGTCCTGA-3′]) were chosen based on (1) the proximity of their targeted sequence to the start codon of the *mPlk4* uORF1 and uORF2, (2) the available PAM sites, and (3) the minimal number of predicted off-target sites according to the CRISPOR website (http://www.crispor.tefor.net). sgRNAs were coinjected with a ssDNA repair template containing the desired modification (ATG start codons of uORF1 and uORF2 were changed to ATA). The repair template (synthesized by IDT) contained a 5′ homology arm (100 bp) and 3′ homology arm (71 bp) flanking the region between the two sgRNA cut sites. The sequence of the repair template was 5′-CGGCGCCCGGGGCTC GGCCTTCTCGCAGTCCCTCCGAGGCAGCGCTCCGAGAA GCCAGCAGGTCTTGGCGCCtATCAGGACGCCTTCTCTAC GCCGCCGCTGGCGACGCCGCCAACGCCACCGAAAGGTA CCCCCGGTACCTCCCGAGGCCTGGGCGGCGCCCCGGAG CTCCtATTTTGAAAAATTCCCGCCGGTCTCCGAACGAGC CAGCCTGGCGGTGACGTCAGCACACTCTCCACTTCTTAG AGGCGGAGACCGACACGCATGCGCAGCAGGG-3′. Pronuclear injection of one-cell B6SJL/F2 embryos (Jackson Laboratories) was performed by the Johns Hopkins University Transgenic Core using a mix of 30 ng/µL Cas9 protein (PNABio), 0.6 µM tracrRNA (Dharmacon), 0.6 µM crRNA (IDT), and 10 ng/µL ssDNA oligonucleotide (IDT) diluted in RNase-free injection buffer (10 mM Tris-HCl at pH 7.4, 0.25 mM EDTA). Injected embryos were transferred into the oviducts of pseudopregnant females. Offspring resulting from embryo injections were tail-clipped at weaning age, and genomic DNA was collected. The following primers were used for PCR amplification of the genomic DNA and sequencing to check for precise editing: mPLK4 5′genomic Fwd (5′-ACACTGACCGCTTTC CG-3′) and mPLK4 uORFs common Rev (5′-CTCGATCCTCTC CCCGA-3′).

Founder mice were bred with C57BL/6J mice, and offspring were screened to verify germline transmission of mutations.

Plk4$^{u1/u1}$ mice were generated alongside *Plk4*$^{\Delta u/\Delta u}$ animals using the same CRISPR/Cas9 approach as described above. Specifically, we identified a single offspring carrying a *u1* allele (the start codon of uORF2 was changed from ATG to ATA, while uORF1 remained intact) following the same injection procedure. This founder mouse was bred with C57BL/6J mice, and offspring were screened to verify germline transmission of mutations.

Plk4$^{+/-}$ mice were generated using CRISPR/Cas9 using a method similar to that described above. To generate a conditional *Plk4*^{flox} allele, two sgRNAs (mPLK4 sgRNA1 [5′-AAGCTAGG ACTTTAATACTC-3′] and mPLK4 sgRNA2 [5′-CTGCATGTAG AGGGAAGCTG-3′]) were used to target the introns flanking exon 5 of the *Plk4* gene. The sgRNAs were coinjected with a repair template that contained 72–100 bp of homology flanking the two *loxP* sites. The sequence of the repair template was 5′-TACAATT AGGCAATAAAACTACTGTTCATATCAGAAGGCAGTCAG TATCACAGCTATTCCTCACTCAGCCCCAGATAACTTCGT ATAATGTATGCTATACGAAGTTATCTTCCCTCTACATGC AGCTATTAGTCCTTTAGCGATCAAACTTGTTCAATAAG TTTAAAAGATTATCCTTATACTGCTCAGTCATTATACGG TCTTTCAAAAGATCCTTAACTATTGGCTGTTTGGTGTTT AATGAAGTTAAAACATTGACATTGCTTTTGGTGGGTGA ATACCTGTGTTGATTTTCATCCAGTGATCTTCTAGGCTT TGAAAGCATTTCTACTGAGTGACAACGTTCTACTGAGT ATGTTTTTGCTCGAGACTGATTAGAGGGGCTGGCTCTA TCAGAGGAATGAGCTCTGCGCAGGTATCGAGAATGCG GCCTCTCTTCTGCATCTTCAATCACTCTCCCCCGTCCCC TACTATTAGCTTCTTGTTCTGGATTTCCCCATTGAGTAC AAAAATTACTTCCATCTCCTGAAGAAAAGTCACTTGAA TTTTTATTTTTTTGAAATACAGTAATTTTATTTGGAAGT GGTTGACCAACCAAAAGTCTTCTGTCAAGTAGGCTGCC ACTCAAACTGGTACCAGAAGAGGCTGTAATTGTTGTGG AAAGTGTAGCATGCCCACTATCCATTGAGTCCTCTACA GTCCCTACGTCTTTACTCTTTGGTGAAGGATTTCGTGA CATGAAAGGATGGTCCAACACAGAAGACAGACTTAACC GATCTGCAGGGTTTCTACGAAGTAACTGGTGGATAAGG TCCTGGGCCTCTCGTGACAAAAAGGCTGGCATTTCATA ATCTGCCAGGACTACTTTGTTCAATGTGTTCTTGACTG TGTCAGTGTCAAAAGGTGGTCTTCCAATAAGTAACGTA TAAAACATACAGCCCAATGACCAAATATCAGATTCAAG TCCATGTGCACTTCGAGTTGCAATTTCTGGTGAAATAT AATTAGGAGTCCCACAGAGTGTATAGTGCTTTTCATGT GGCATATTCAACTGCGTTGCTAGTCCAAAGTCAGCAAT TTTTATGTTCATATTCCGCGTAAGTAAGATGTTAGAGA GTGTGAGGTCCCGGTGCAATATGCCATGAGAATGAAG ATATAACATTCCTGTGATAATCTGGTGCATGAAGTGCC TAGCTGTGAAGATAGAAAAAGAGAGAGCTTAACAATTC AAATCTGGGAAATTTATTGTTTAGAATACACGATAAAA TCTAGTATACACGCCAGAGATAACTTCGTATAATGTAT

GCTATACGAAGTTATTATTAAAGTCCTAGCTTGCAGGT
TAGATTTATCAACTAAAACACCATTCTATCAATATAATG
CTATCTAATTCCCCTCAAGAAAACTAGACACTCCTTTT-3′.

The following primers were used for PCR amplification to screen for precise editing: 976 Plk4_F (5′-TCTTGAGGGGAAT TAGATAGCA-3′), 979 Plk4_R (loxP; 5′-CTCACTCAGCCCCA GATAAC-3′), and 981 Plk4_R (5′-TGCAATATGCCATGAG AATGA-3′).

Founder mice were bred with C57BL/6J mice, and offspring were screened to verify germline transmission of mutations. *Plk4*$^{f/+}$ F2 animals were then crossed to Sox2-Cre animals obtained from the Jackson Laboratory (008454), to generate the *PLK4*$^{+/-}$ line.

Centrin-GFP mice were obtained from the laboratory of D. Cleveland (University of California at San Diego; Jax 029363). The following primers were used for genotyping: centrin-GFP-Rosa-P1 (5′-AAAGTCGCTCTGAGTTGTTAT-3′), centrin-GFP-Rosa-P2 (5′-GCGAAGAGTTTGTCCTCAACC-3′), and centrin-GFP-Rosa-P3 (5′-GGAGCGGGAGAAATGGATATG-3′).

Analysis of all animals was performed on a mixed C57BL/6J and SJL/J background. Genotyping was carried out using standard PCR protocols. Embryos and adults from both genders were included in our analysis unless indicated otherwise. Mice were housed and cared for in an AAALAC-accredited facility, and all animal experiments were conducted in accordance with Institutional Animal Care and Use Committee-approved protocols. Details on sgRNA, repair template, and genotyping primers are also listed in Supplemental Table S2.

Fertility analysis

To monitor fertility, each 4- to 5-wk-old male or female mouse was paired with a wild-type animal and constantly maintained with the same breeding partner. The frequency of each litter and the number of pups per litter were closely monitored during the subsequent 5–6 mo.

Sperm analysis

Sperm isolation To isolate sperm for analysis, the epididymides were harvested and transferred to 5 mL of EmbryoMax human tubal fluid (Millipore Sigma MR-070-D) preheated to 37°C. The epididymides were cut several times along the tube length and then incubated for 30 min at 37°C to release the sperm into solution. Next, the supernatant was collected in a 15-mL conical tube and centrifuged at 600 rpm for 5 min. The tube was then placed upright for 15 min in a 37°C incubator. The top 4 mL of supernatant was transferred to a new conical tube and centrifuged at 4000 rpm for 10 min. Immediately following centrifugation, the top 3 mL of supernatant was removed, leaving the bottom 1 mL of concentrated sperm. The sperm was maintained for up to 1 h at 37°C before being analyzed.

Sperm count Sperm count was measured using a hemacytometer. Images of concentrated sperm solution loaded into a hemacytometer were taken using a digital camera (MU1003) attached to a bright-field microscope with a Nikon Eclipse TS100 10×, 0.25 NA air objective. The number of sperm per field of view was quantified using ImageJ software (National Institutes of Health).

Sperm motility Approximately 50 µL of sperm solution of a concentration range of 1×10^4 to 7×10^5 was loaded between two glass coverslips to limit the field of view to a single layer of motile sperm. Sperm movement was captured using time-lapse movies with a digital camera (MU1003) attached to a bright-field microscope with a Nikon Eclipse TS100 10×, 0.25 NA air objective. Movies were visualized with ImageJ software (National Institutes of Health), and sperm motility was quantified in the Matlab program.

Sperm flagellum length measurement Sperm were spun onto charged glass slides (Thermo Fisher Scientific) at 500 rpm for 5 min using a Thermo Shandon Cytospin3 centrifuge. Sperm were then fixed with 1.5% PFA (diluted in 1× PBS) for 4 min at room temperature and then submerged in ice-cold methanol for 4 min at −20°C. Slides were then washed three times with 1× PBS for 5 min before blocking with antibody dilution buffer (ADB; 50 mL of PBS, 3% BSA, 10% goat or horse serum, 0.05% Triton X-100) and incubated overnight at 37°C. The next day, the primary antibody mouse acetylated α-tubulin (1:1000; Cell Signaling 12151S) diluted in ADB was applied for 1 h at 37°C. Slides were washed once with PBS for 5 min before secondary antibodies and DAPI (diluted in ADB) were added for 1 h at 37°C. Glass coverslips were mounted using ProLong Gold antifade mountant (Invitrogen). Secondary antibodies were conjugated to Alexa fluor 488, 555, or 647 (1:1000; Thermo Fisher Scientific). Details on antibodies are also listed in Supplemental Table S1.

Immunofluorescence images were acquired using a DeltaVision Elite system (GE Healthcare) controlling a scientific CMOS camera (pco.edge 5.5). Images were acquired using an Olympus 40×, 1.35 NA oil objective with Applied Precision immersion oil ($n = 1.516$) at 40× with 0.2-µm z-sections. Images were visualized with ImageJ software, and tail length was measured from the base of the sperm head to the end of the flagellum.

Mouse tissue sectioning, immunohistochemistry, and histological analysis

Adult mouse tissues were harvested, embedded fresh into OCT medium, and frozen for cryosectioning. Twenty-micrometer tissue sections were cut using a Leica CM1950 cryostat and collected on Superfrost Plus microscope slides (Thermo Fisher Scientific).

For immunohistochemistry staining experiments of embryonic gonads, whole embryos were harvested, embedded fresh into OCT medium, and frozen for cryosectioning. Ten-micrometer tissue sections were cut using a Leica CM1950 cryostat and collected on Superfrost Plus microscope slides (Thermo Fisher Scientific). To determine the sex of each embryo, the following primers were used to determine the presence of the SRY gene: SRY Fwd (5′-TTGTCTAGAGAGCATGGAGGGCCATGTCAA-3′) and SRY Rev (5′-CCACTCCTCTGTGACACTTTAGCCCTCCGA-3′).

For immunohistochemistry staining, the tissue sections were fixed in 1.5%–4% paraformaldehyde (Electron Microscopy Sciences) diluted in PBS for 8 min at room temperature. Tissue sections were then washed with PBS and permeabilized/blocked with blocking solution (10% donkey serum [Sigma Aldrich], 0.1%–0.5% Triton X-100 in PBS) for 1 h at room temperature. Next, tissue sections were incubated with the respective primary antibodies diluted in blocking solution for 1.5 h at room temperature or overnight at 4°C. The following primary antibodies were used: rabbit DAZL (1:500; Abcam ab215718), mouse SYCP3 (1:250; Santa Cruz Biotechnology sc-74568), rabbit DDX4 (1:500; Abcam ab13840), rabbit OCT4 (1:250; Abcam ab181557), goat γ-tubulin (1:500; homemade, polyclonal, raised against the peptide CDEYHAATRPDYISWGTQEQ), and rabbit CEP164 (1:500; EMD Millipore ABE2621). Following primary antibody staining, the tissue slides were washed three times with PBST (0.1% Triton X-100) and incubated with secondary antibodies and DAPI diluted in blocking solution for 1 h at room

temperature. Following secondary antibody staining, the tissue slides were washed three times with PBST before mounting. Secondary antibodies were conjugated to Alexa fluor 488, 555, or 647 (1:500; Thermo Fisher Scientific). Details on antibodies are also listed in Supplemental Table S1. Stained tissue sections were mounted in ProLong Gold antifade (Invitrogen). Images of stained sections were obtained using an SP8 (Leica Microsystems) confocal microscope. For centriole visualization, images were collected using a Leica 63×, 1.40 NA oil or 40×, 1.30 NA oil objective with 0.25-µm z-sections. For all other staining, images were collected using a Leica 40×, 1.30 NA oil objective with 1- to 2-µm z-sections.

For histological assessment, mouse testes and ovaries were fixed overnight in Bouin's fixative (Ricca Chemical Company). The next day, the tissues were washed with 70%, 90%, and 100% EtOH solutions prior to shipment to AML Laboratories for paraffin embedding, sectioning (5-µm thickness), and hematoxylin and eosin (H&E) staining. For all other tissues, the Johns Hopkins University School of Medicine Phenotyping Core performed the tissue processing, paraffin embedding, sectioning (5-µm thickness), and H&E staining. All pathologies were analyzed by a certified veterinary pathologist. Images of histological sections were obtained using a Leica 10×, 0.4 NA or 40×, 0.8 NA air objective.

Ultrastructure expansion microscopy of embryonic gonads

Tissue fixation, gelation, and punching Using a hydrophobic barrier pen (Vector Laboratories), a hydrophobic boundary was drawn around the 10-µm embryonic gonad sections collected on Superfrost Plus microscope slides (Thermo Fisher Scientific). The tissue was then fixed in anchoring solution containing 0.7% paraformaldehyde (Electron Microscopy Sciences) and 1% acrylamide (Bio-Rad) diluted in 1× PBS overnight at 37°C. The next day, precooled gelation reagents were combined in chilled 1× PBS at the following final concentrations: 10% acrylamide, 23% sodium acrylate (AK Scientific), 0.1% bis-acrylamide (Bio-Rad), 0.5% APS (Sigma), and 0.5% TEMED (Sigma), with APS and TEMED added just before application. Gelling solution was quickly transferred to the tissue slide, incubated for 1 h on ice, and then moved for 3–4 h to 37°C. Following gel polymerization, a 4-mm biopsy punch (Integra Miltex) was used to excise a single punch that fully encompassed the gonad tissue.

Denaturation and first round of expansion Punches were incubated with denaturation buffer (200 mM SDS, 200 mM NaCl, 50 mM TRIS at pH 9) for 10 min at room temperature with gentle agitation before transferring to denaturation buffer that had been preheated to >90°C. Punches were maintained in denaturation buffer for 1 h at >90°C with gentle agitation every 20 min and then allowed to cool overnight at room temperature. The next day, denaturation buffer was removed by exchanging with ddH_2O every 30 min five to six times. Punches were then allowed to expand to approximately four times in size overnight at room temperature with gentle agitation.

Immunostaining The next day, punches were transferred to 1× PBS, which was exchanged every 20 min three to four times or until punches were reduced from approximately four to two times in size. Punches were then blocked in blocking solution (1% BSA, 0.05% Tween-20 in PBS) for 30 min at room temperature, followed by incubation with primary antibody diluted in blocking solution for 3 h at 37°C with constant agitation. Punches were washed three times in PBST (0.1% Tween-20) for 30 min. Punches were then incubated for 3 h at 37°C with secondary antibody and DAPI (diluted 1:500; Millipore Sigma) diluted in blocking solution with constant agitation. The following primary antibodies were used for immunostaining of expanded samples: mouse acetylated tubulin (1:500; Santa Cruz Biotechnology sc-23950), rabbit GFP (1:250; Amsbio TP401), and rabbit DDX4 (1:500; Abcam ab13840). Secondary antibodies were conjugated to Alexa fluor 488, 555, or 647 (1:500; Thermo Fisher Scientific). Details on antibodies are also listed in Supplemental Table S1.

Second round of expansion, mounting, and imaging After immunostaining, punches were washed three times in PBST (0.1% Tween-20) for 30 min, followed by three washes with dH_2O for 1–2 h. The punches were expanded a second time in dH_2O overnight at room temperature with gentle agitation. Prior to imaging, expanded punches were measured using an electronic caliper (Fowler-Sylvac) to determine the degree of expansion before mounting onto 35-mm glass-bottom microwell dishes (Celvis). For centriole visualization, images were collected using a Leica 63×, 1.40 NA oil objective with 0.25-µm z-sections.

Single-molecule fluorescence in situ hybridization and immunofluorescence

Cell dissociation from embryonic gonads E13.5 gonads were harvested and incubated in 0.05% Trypsin-EDTA (Thermo Scientific) for 5–10 min at 37°C prior to dissociation by pipetting. Dissociated cells were spun onto charged glass slides (Thermo Fisher Scientific) at 300 rpm for 5 min using a Thermo Shandon Cytospin3 centrifuge.

Probe hybridization, immunofluorescent staining, and imaging Reagents and the detailed protocol for smFISH and IF were described in Lyubimova et al. (2013). Briefly, cells were fixed with 4% PFA (diluted in 1× PBS), permeabilized with permeabilization buffer (1× PBS, 5 mM $MgCl_2$, 0.5% Triton), and incubated with prehybridization buffer (2× SSC, 15% formamide). Cells were incubated with fluorescently labeled PLK4-Cy3 (80 nM) smFISH probes and rabbit DDX4 (1:250; Abcam ab13840) antibody diluted in hybridization buffer for 3 h at 37°C. Oligonucleotide probe sequences are listed in Supplemental Table S2. Following washes, cells were incubated with Alexa fluor 488 secondary antibody (Life Technologies) diluted in hybridization buffer for 1 h at room temperature. Cells were mounted using ProLong Diamond antifade reagent with DAPI (Life Technologies). For single-molecule mRNA visualization, images were collected using a Leica 63×, 1.40 NA oil with 0.2-µm z-sections.

Image and movie analysis

ImageJ software (National Institutes of Health) was used for all image and movie analysis from cultured cells and isolated sperm. LAX software (Leica) was used for all image analysis of histology sections and tissue staining.

For quantitation of signal intensity at the centrosome, deconvolved 2D maximum intensity projections were saved as 16-bit TIFF images. Signal intensity was determined by drawing a circular region of interest (ROI) around the centriole (small ROI [ROI_S]). A larger concentric circle (large ROI [ROI_L]) was drawn around ROI_S. ROI_S and ROI_L were transferred to the channel of interest, and the signal in ROI_S was calculated using the formula $I_S - [(I_L - I_S)/(A_L - A_S) \times A_S]$, where A is area and I is integrated intensity.

For quantification of signal intensity of the nucleus from time-lapse movies, deconvolved 2D maximum intensity projections were saved as 16-bit TIFF images. The average background

intensity per pixel (P_B) was calculated from 10 different regions without any cells. Nuclear area was determined by drawing an outline of the nucleus (nuclear ROI [ROI_N]) in the iRFP-PCNA channel. The outlined region was transferred to the channel of interest, and signal intensity was calculated using the formula $I_N - [(P_N - P_B) \times A_N]$, where A is area, I is integrated intensity, and P is average intensity per pixel.

For nuclear size and circularity analysis, lightning-processed 2D maximum intensity projections were saved as 16-bit TIFF images. Nuclear area was determined by drawing an outline of the nucleus (nuclear ROI [ROI_N]) in the DAPI channel. The circularity of ROI_N was calculated using the formula $(4\pi \times A_N)/P_N^2$, where A is area and P is the perimeter of the outlined nucleus.

For smFISH analysis, lightning-processed 2D maximum intensity projections were saved as 16-bit TIFF images. The number of PLK4 mRNA foci was quantified for individual cells.

Quantitative real-time PCR and cDNA sequencing

Total RNA was isolated from cells or homogenized tissue using Trizol reagent (Thermo Fisher Scientific). For all reporter cell lines, RNA isolation following Trizol homogenization was performed using the RNeasy mini kit (Qiagen). Isolated RNA was converted to cDNA using SuperScript IV reverse transcriptase (Thermo Fisher Scientific) with oligo dT primers. Quantitative real-time PCR was performed using Ssoadvanced Universal SYBR (Bio-Rad) on a QuantStudio 6 Flex real-time PCR system (Thermo Fisher Scientific). Analysis was performed using the QuantStudio real-time PCR software. Reactions were carried out in technical triplicate. Details on primers used are listed in Supplemental Table S2.

For measurements of the human uORF and 5′ UTR reporter mRNA expression (Fig. 1C), the following primers were used: EGFP Fwd (5′-AAGGGCATCGACTTCAAGG-3′) and EGFP Rev (5′-TCCAGCAGGACCATGTGATCGC-3′).

For measurements of the human truncated PLK4 reporter mRNA expression (Supplemental Fig. S1F), the following primers were used: truncated hPLK4 Fwd (5′-TCGGGGAGAAGATCGA GGATTTTAAAG-3′) and truncated hPLK4 Rev (5′-GCACCA CCCCGGTGAACA-3′).

For measurements of the human full-length PLK4 reporter mRNA expression (Fig. 1I), the following primers were used: full-length hPLK4 Fwd (5′-TTTGATGTTTTCTAATCCGAC TCCTAA-3′) and full-length hPLK4 Rev (5′-GCCGGTGGTGCA GAT-3′).

For measurements of the human GAPDH mRNA expression (Fig. 1C,I; Supplemental Fig. S1F), the following primers were used: hGADPH Fwd (5′-ACAGTCCATGCCATCACTGCC-3′) and hGADPH Rev (5′-GCCTGCTTCACCACCTTCTTG-3′).

For measurements of the endogenous mouse PLK4 mRNA expression (Fig. 5B), the following primers were used: mPLK4 Fwd (5′-CCGGGACCTCACACTCTCTA-3′) and mPLK4 Rev (5′-TCGAGTTGCAATTTCTGGTG-3′).

For measurements of the mouse GAPDH mRNA expression (Fig. 5B), the following primers were used: mGADPH Fwd (5′-AATGTGTCCGTCGTGGATCTGA-3′) and mGADPH Rev (5′-TGGGAGTTGCTGTTGAAGTCG-3′).

PLK4 expression levels were normalized to GADPH. The fold changes in mRNA expression were calculated using the $2^{-\Delta\Delta Ct}$ method, and expression values were expressed as fold increase in the average expression compared with mORF controls (Fig. 1C), uORF1+2 controls (Fig. 1I; Supplemental Fig. S1F) for reporter cell lines, or $Plk4^{+/+}$ controls (Fig. 5B) for MEFs.

For sequencing of the cDNA from MEFs (Fig. 5C), the following primers were used to amplify a region containing both uORFs: mPlk4 uORFs Fwd (5′-CTCTAAGAAGTGGAGAGTGTGC-3′) and mPlk4 exon 3 Rev (5′-TCACCTCATTTTGGACTCTCTG-3′).

The amplicon was purified and used for Sanger sequencing. Sequences were visualized with SnapGene.

Statistical analysis

Statistical analysis was performed using GraphPad Prism software. Differences between samples were analyzed using a two-tailed unpaired Student's *t*-tests (Welch's *t*-test), χ^2 test with post-hoc analysis, or one-way ANOVA with post-hoc analysis as indicated in the figure legends. Error bars represent SEM unless otherwise indicated. Figure legends state the number of animals/biological replicates, cells/seminiferous tubules, and technical replicates per experiment. Details on all statistical analysis are described in Supplemental Table S3. All raw data values are listed in Supplemental Table S4.

Data availability

This study includes no data deposited in external repositories.

Competing interest statement

The authors declare no competing interests.

Acknowledgments

We thank the members of the Holland laboratory, the Regot laboratory, the Green laboratory, the Wu laboratory, and the Hajkova laboratory for their valuable insights and technical support. We thank Dr. Cory Brayton for pathological analysis of all mouse tissues in this study. This work was supported by the National Institutes of Health (NIH) grants R01CA266199, R01GM114119, and R01GM133897 to A.J.H, and National Institute of General Medical Sciences grant R01GM11755 to P.W.J. M.W.S. was supported by a training grant fellowship from the National Cancer Institute (NCI, NIH; T32CA009110). T.P.P was supported by NIH training grant T32GM007445.

Author contributions: T.P.P. performed and analyzed the majority of the experiments and prepared the figures. C.A.B., C.G.D., and M.A.S. assisted with animal husbandry. C.A.B. assisted with cloning and analysis of experiments with reporter cell lines. C.G.D. assisted with sperm analysis, dissection, and analysis of adult and embryonic tissues. M.W.S. and P.W.J. helped perform the initial characterization of the fertility defects in $Plk4^{\Delta u/\Delta u}$ male animals. A.J.H. and T.P.P. wrote the manuscript. All authors edited the manuscript. A.J.H. conceived and supervised the study.

References

Aitken RJ, Findlay JK, Hutt KJ, Kerr JB. 2011. Apoptosis in the germ line. *Reproduction* **141:** 139–150. doi:10.1530/REP-10-0232

Andreev DE, O'Connor PB, Fahey C, Kenny EM, Terenin IM, Dmitriev SE, Cormican P, Morris DW, Shatsky IN, Baranov PV. 2015. Translation of 5′ leaders is pervasive in genes resistant to eIF2 repression. *Elife* **4:** e03971. doi:10.7554/eLife.03971

Baird TD, Palam LR, Fusakio ME, Willy JA, Davis CM, McClintick JN, Anthony TG, Wek RC. 2014. Selective mRNA translation during eIF2 phosphorylation induces expression of IBTKα. *Mol Biol Cell* **25:** 1686–1697. doi:10.1091/mbc.e14-02-0704

Bao J, Yu Y, Chen J, He Y, Chen X, Ren Z, Xue C, Liu L, Hu Q, Li J, et al. 2018. MiR-126 negatively regulates PLK-4 to impact the development of hepatocellular carcinoma via ATR/CHEK1 pathway. *Cell Death Dis* **9:** 1045. doi:10.1038/s41419-018-1020-0

Barbosa C, Peixeiro I, Romão L. 2013. Gene expression regulation by upstream open reading frames and human disease. *PLoS Genet* **9:** e1003529. doi:10.1371/journal.pgen.1003529

Bettencourt-Dias M, Rodrigues-Martins A, Carpenter L, Riparbelli M, Lehmann L, Gatt MK, Carmo N, Balloux F, Callaini G, Glover DM. 2005. SAK/PLK4 is required for centriole duplication and flagella development. *Curr Biol* **15:** 2199–2207. doi:10.1016/j.cub.2005.11.042

Breslow DK, Holland AJ. 2019. Mechanism and regulation of centriole and cilium biogenesis. *Annu Rev Biochem* **88:** 691–724. doi:10.1146/annurev-biochem-013118-111153

Cajanek L, Glatter T, Nigg EA. 2015. The E3 ubiquitin ligase Mib1 regulates Plk4 and centriole biogenesis. *J Cell Sci* **128:** 1674–1682. doi:10.1242/jcs.166496

Chavali PL, Pütz M, Gergely F. 2014. Small organelle, big responsibility: the role of centrosomes in development and disease. *Philos Trans R Soc Lond B Biol Sci* **369:** 20130468. doi:10.1098/rstb.2013.0468

Cizmecioglu O, Arnold M, Bahtz R, Settele F, Ehret L, Haselmann-Weiß U, Antony C, Hoffmann I. 2010. Cep152 acts as a scaffold for recruitment of Plk4 and CPAP to the centrosome. *J Cell Biol* **191:** 731–739. doi:10.1083/jcb.201007107

Coelho PA, Bury L, Shahbazi MN, Liakath-Ali K, Tate PH, Wormald S, Hindley CJ, Huch M, Archer J, Skarnes WC, et al. 2015. Over-expression of Plk4 induces centrosome amplification, loss of primary cilia and associated tissue hyperplasia in the mouse. *Open Biol* **5:** 150209. doi:10.1098/rsob.150209

Cunha-Ferreira I, Rodrigues-Martins A, Bento I, Riparbelli M, Zhang W, Laue E, Callaini G, Glover DM, Bettencourt-Dias M. 2009. The SCF/Slimb ubiquitin ligase limits centrosome amplification through degradation of SAK/PLK4. *Curr Biol* **19:** 43–49. doi:10.1016/j.cub.2008.11.037

Cunha-Ferreira I, Bento I, Pimenta-Marques A, Jana SC, Lince-Faria M, Duarte P, Borrego-Pinto J, Gilberto S, Amado T, Brito D, et al. 2013. Regulation of autophosphorylation controls PLK4 self-destruction and centriole number. *Curr Biol* **23:** 2245–2254. doi:10.1016/j.cub.2013.09.037

Czechanski A, Kim H, Byers C, Greenstein I, Stumpff J, Reinholdt LG. 2015. Kif18a is specifically required for mitotic progression during germ line development. *Dev Biol* **402:** 253–262. doi:10.1016/j.ydbio.2015.03.011

Dzhindzhev NS, Tzolovsky G, Lipinszki Z, Abdelaziz M, Debski J, Dadlez M, Glover DM. 2017. Two-step phosphorylation of Ana2 by Plk4 is required for the sequential loading of Ana2 and Sas6 to initiate procentriole formation. *Open Biol* **7:** 170247. doi:10.1098/rsob.170247

Fan G, Sun L, Shan P, Zhang X, Huan J, Zhang X, Li D, Wang T, Wei T, Zhang X, et al. 2015. Loss of KLF14 triggers centrosome amplification and tumorigenesis. *Nat Commun* **6:** 8450. doi:10.1038/ncomms9450

Fischer M, Quaas M, Wintsche A, Müller GA, Engeland K. 2014. Polo-like kinase 4 transcription is activated via CRE and NRF1 elements, repressed by DREAM through CDE/CHR sites and deregulated by HPV E7 protein. *Nucleic Acids Res* **42:** 163–180. doi:10.1093/nar/gkt849

Ganem NJ, Godinho SA, Pellman D. 2009. A mechanism linking extra centrosomes to chromosomal instability. *Nature* **460:** 278–282. doi:10.1038/nature08136

Gao X, Wan J, Liu B, Ma M, Shen B, Qian SB. 2015. Quantitative profiling of initiating ribosomes in vivo. *Nat Methods* **12:** 147–153. doi:10.1038/nmeth.3208

Guderian G, Westendorf J, Uldschmid A, Nigg EA. 2010. Plk4 trans-autophosphorylation regulates centriole number by controlling βTrCP-mediated degradation. *J Cell Sci* **123:** 2163–2169. doi:10.1242/jcs.068502

Habedanck R, Stierhof YD, Wilkinson CJ, Nigg EA. 2005. The Polo kinase Plk4 functions in centriole duplication. *Nat Cell Biol* **7:** 1140–1146. doi:10.1038/ncb1320

Hajkova P, Ancelin K, Waldmann T, Lacoste N, Lange UC, Cesari F, Lee C, Almouzni G, Schneider R, Surani MA. 2008. Chromatin dynamics during epigenetic reprogramming in the mouse germ line. *Nature* **452:** 877–881. doi:10.1038/nature06714

Han K, Jaimovich A, Dey G, Ruggero D, Meyuhas O, Sonenberg N, Meyer T. 2014. Parallel measurement of dynamic changes in translation rates in single cells. *Nat Methods* **11:** 86–93. doi:10.1038/nmeth.2729

Harding HP, Novoa I, Zhang Y, Zeng H, Wek R, Schapira M, Ron D. 2000. Regulated translation initiation controls stress-induced gene expression in mammalian cells. *Mol Cell* **6:** 1099–1108. doi:10.1016/S1097-2765(00)00108-8

Harris RM, Weiss J, Jameson JL. 2011. Male hypogonadism and germ cell loss caused by a mutation in polo-like kinase 4. *Endocrinology* **152:** 3975–3985. doi:10.1210/en.2011-1106

Hatch EM, Kulukian A, Holland AJ, Cleveland DW, Stearns T. 2010. Cep152 interacts with Plk4 and is required for centriole duplication. *J Cell Biol* **191:** 721–729. doi:10.1083/jcb.201006049

Holland AJ, Lan W, Niessen S, Hoover H, Cleveland DW. 2010. Polo-like kinase 4 kinase activity limits centrosome overduplication by autoregulating its own stability. *J Cell Biol* **188:** 191–198. doi:10.1083/jcb.200911102

Holland AJ, Fachinetti D, Zhu Q, Bauer M, Verma IM, Nigg EA, Cleveland DW. 2012. The autoregulated instability of polo-like kinase 4 limits centrosome duplication to once per cell cycle. *Genes Dev* **26:** 2684–2689. doi:10.1101/gad.207027.112

Iwamoto M, Björklund T, Lundberg C, Kirik D, Wandless TJ. 2010. A general chemical method to regulate protein stability in the mammalian central nervous system. *Chem Biol* **17:** 981–988. doi:10.1016/j.chembiol.2010.07.009

Jayaraman D, Bae BI, Walsh CA. 2018. The genetics of primary microcephaly. *Annu Rev Genomics Hum Genet* **19:** 177–200. doi:10.1146/annurev-genom-083117-021441

Kim TS, Park JE, Shukla A, Choi S, Murugan RN, Lee JH, Ahn M, Rhee K, Bang JK, Kim BY, et al. 2013. Hierarchical recruitment of Plk4 and regulation of centriole biogenesis by two centrosomal scaffolds, Cep192 and Cep152. *Proc Natl Acad Sci* **110:** E4849–E4857. doi:10.1073/pnas.1319656110

Klebba JE, Buster DW, Nguyen AL, Swatkoski S, Gucek M, Rusan NM, Rogers GC. 2013. Polo-like kinase 4 autodestructs by generating its slimb-binding phosphodegron. *Curr Biol* **23:** 2255–2261. doi:10.1016/j.cub.2013.09.019

Kozak M. 1987. An analysis of 5′-noncoding sequences from 699 vertebrate messenger RNAs. *Nucleic Acids Res* **15:** 8125–8148. doi:10.1093/nar/15.20.8125

Kozak M. 1991. An analysis of vertebrate mRNA sequences: intimations of translational control. *J Cell Biol* **115:** 887–903. doi:10.1083/jcb.115.4.887

Kozak M. 2001. Constraints on reinitiation of translation in mammals. *Nucleic Acids Res* **29:** 5226–5232. doi:10.1093/nar/29.24.5226

Kozak M. 2002. Pushing the limits of the scanning mechanism for initiation of translation. *Gene* **299:** 1–34. doi:10.1016/S0378-1119(02)01056-9

Laird DJ, Altshuler-Keylin S, Kissner MD, Zhou X, Anderson KV. 2011. Ror2 enhances polarity and directional migration of primordial germ cells. *PLoS Genet* **7:** e1002428. doi:10.1371/journal.pgen.1002428

Ledoux AC, Sellier H, Gillies K, Iannetti A, James J, Perkins ND. 2013. NFκB regulates expression of Polo-like kinase 4. *Cell Cycle* **12:** 3052–3062. doi:10.4161/cc.26086

Lee J, Inoue K, Ono R, Ogonuki N, Kohda T, Kaneko-Ishino T, Ogura A, Ishino F. 2002. Erasing genomic imprinting memory in mouse clone embryos produced from day 11.5 primordial germ cells. *Development* **129:** 1807–1817. doi:10.1242/dev.129.8.1807

Lee MY, Moreno CS, Saavedra HI. 2014. E2f activators signal and maintain centrosome amplification in breast cancer cells. *Mol Cell Biol* **34:** 2581–2599. doi:10.1128/MCB.01688-13

Levine MS, Holland AJ. 2018. The impact of mitotic errors on cell proliferation and tumorigenesis. *Genes Dev* **32:** 620–638. doi:10.1101/gad.314351.118

Levine MS, Bakker B, Boeckx B, Moyett J, Lu J, Vitre B, Spierings DC, Lansdorp PM, Cleveland DW, Lambrechts D, et al. 2017. Centrosome amplification is sufficient to promote spontaneous tumorigenesis in mammals. *Dev Cell* **40:** 313–322 e315. doi:10.1016/j.devcel.2016.12.022

Lu PD, Harding HP, Ron D. 2004. Translation reinitiation at alternative open reading frames regulates gene expression in an integrated stress response. *J Cell Biol* **167:** 27–33. doi:10.1083/jcb.200408003

Luukkonen BG, Tan W, Schwartz S. 1995. Efficiency of reinitiation of translation on human immunodeficiency virus type 1 mRNAs is determined by the length of the upstream open reading frame and by intercistronic distance. *J Virol* **69:** 4086–4094. doi:10.1128/jvi.69.7.4086-4094.1995

Lyubimova A, Itzkovitz S, Junker JP, Fan ZP, Wu X, van Oudenaarden A. 2013. Single-molecule mRNA detection and counting in mammalian tissue. *Nat Protoc* **8:** 1743–1758. doi:10.1038/nprot.2013.109

Miyamoto T, Bando Y, Koh E, Tsujimura A, Miyagawa Y, Iijima M, Namiki M, Shiina M, Ogata K, Matsumoto N, et al. 2016. A PLK4 mutation causing azoospermia in a man with Sertoli cell-only syndrome. *Andrology* **4:** 75–81. doi:10.1111/andr.12113

Morris DR, Geballe AP. 2000. Upstream open reading frames as regulators of mRNA translation. *Mol Cell Biol* **20:** 8635–8642. doi:10.1128/MCB.20.23.8635-8642.2000

Nguyen DH, Soygur B, Peng SP, Malki S, Hu G, Laird DJ. 2020. Apoptosis in the fetal testis eliminates developmentally defective germ cell clones. *Nat Cell Biol* **22:** 1423–1435. doi:10.1038/s41556-020-00603-8

Nigg EA, Holland AJ. 2018. Once and only once: mechanisms of centriole duplication and their deregulation in disease. *Nat Rev Mol Cell Biol* **19:** 297–312. doi:10.1038/nrm.2017.127

Ohta M, Ashikawa T, Nozaki Y, Kozuka-Hata H, Goto H, Inagaki M, Oyama M, Kitagawa D. 2014. Direct interaction of Plk4 with STIL ensures formation of a single procentriole per parental centriole. *Nat Commun* **5:** 5267. doi:10.1038/ncomms6267

Park SY, Park JE, Kim TS, Kim JH, Kwak MJ, Ku B, Tian L, Murugan RN, Ahn M, Komiya S, et al. 2014. Molecular basis for unidirectional scaffold switching of human Plk4 in centriole biogenesis. *Nat Struct Mol Biol* **21:** 696–703. doi:10.1038/nsmb.2846

Percharde M, Wong P, Ramalho-Santos M. 2017. Global hypertranscription in the mouse embryonic germline. *Cell Rep* **19:** 1987–1996. doi:10.1016/j.celrep.2017.05.036

Phan TP, Holland AJ. 2021. Time is of the essence: the molecular mechanisms of primary microcephaly. *Genes Dev* **35:** 1551–1578. doi:10.1101/gad.348866.121

Pöyry TA, Kaminski A, Jackson RJ. 2004. What determines whether mammalian ribosomes resume scanning after translation of a short upstream open reading frame? *Genes Dev* **18:** 62–75. doi:10.1101/gad.276504

Reinholdt LG, Munroe RJ, Kamdar S, Schimenti JC. 2006. The mouse gcd2 mutation causes primordial germ cell depletion. *Mech Dev* **123:** 559–569. doi:10.1016/j.mod.2006.05.003

Rogers GC, Rusan NM, Roberts DM, Peifer M, Rogers SL. 2009. The SCF Slimb ubiquitin ligase regulates Plk4/Sak levels to block centriole reduplication. *J Cell Biol* **184:** 225–239. doi:10.1083/jcb.200808049

Runyan C, Schaible K, Molyneaux K, Wang Z, Levin L, Wylie C. 2006. Steel factor controls midline cell death of primordial germ cells and is essential for their normal proliferation and migration. *Development* **133:** 4861–4869. doi:10.1242/dev.02688

Ryniawec JM, Rogers GC. 2021. Centrosome instability: when good centrosomes go bad. *Cell Mol Life Sci* **78:** 6775–6795. doi:10.1007/s00018-021-03928-1

Saitou M, Yamaji M. 2012. Primordial germ cells in mice. *Cold Spring Harb Perspect Biol* **4:** a008375. doi:10.1101/cshperspect.a008375

Saitou M, Kagiwada S, Kurimoto K. 2012. Epigenetic reprogramming in mouse pre-implantation development and primordial germ cells. *Development* **139:** 15–31. doi:10.1242/dev.050849

Seki Y, Hayashi K, Itoh K, Mizugaki M, Saitou M, Matsui Y. 2005. Extensive and orderly reprogramming of genome-wide chromatin modifications associated with specification and early development of germ cells in mice. *Dev Biol* **278:** 440–458. doi:10.1016/j.ydbio.2004.11.025

Seki Y, Yamaji M, Yabuta Y, Sano M, Shigeta M, Matsui Y, Saga Y, Tachibana M, Shinkai Y, Saitou M. 2007. Cellular dynamics associated with the genome-wide epigenetic reprogramming in migrating primordial germ cells in mice. *Development* **134:** 2627–2638. doi:10.1242/dev.005611

Sepaniac LA, Martin W, Dionne LA, Stearns TM, Reinholdt LG, Stumpff J. 2021. Micronuclei in Kif18a mutant mice form stable micronuclear envelopes and do not promote tumorigenesis. *J Cell Biol* **220:** e202101165. doi:10.1083/jcb.202101165

Serçin O, Larsimont JC, Karambelas AE, Marthiens V, Moers V, Boeckx B, Le Mercier M, Lambrechts D, Basto R, Blanpain C. 2016. Transient PLK4 overexpression accelerates tumorigenesis in p53-deficient epidermis. *Nat Cell Biol* **18:** 100–110. doi:10.1038/ncb3270

Silkworth WT, Nardi IK, Scholl LM, Cimini D. 2009. Multipolar spindle pole coalescence is a major source of kinetochore mis-attachment and chromosome mis-segregation in cancer cells. *PLoS ONE* **4:** e6564. doi:10.1371/journal.pone.0006564

Sonnen KF, Schermelleh L, Leonhardt H, Nigg EA. 2012. 3D-structured illumination microscopy provides novel insight into architecture of human centrosomes. *Biol Open* **1:** 965–976. doi:10.1242/bio.20122337

Sonnen KF, Gabryjonczyk AM, Anselm E, Stierhof YD, Nigg EA. 2013. Human Cep192 and Cep152 cooperate in Plk4 recruitment and centriole duplication. *J Cell Sci* **126:** 3223–3233. doi:10.1242/jcs.129502

Tam PP, Snow MH. 1981. Proliferation and migration of primordial germ cells during compensatory growth in mouse embryos. *J Embryol Exp Morphol* **64:** 133–147.

Vattem KM, Wek RC. 2004. Reinitiation involving upstream ORFs regulates ATF4 mRNA translation in mammalian cells. *Proc Natl Acad Sci* **101:** 11269–11274. doi:10.1073/pnas.0400541101

Wang JT, Stearns T. 2018. The ABCs of centriole architecture: the form and function of triplet microtubules. *Cold Spring Harb Symp Quant Biol* **82:**145–155. doi:10.1101/sqb.2017.82.034496

Wang RA, Nakane PK, Koji T. 1998. Autonomous cell death of mouse male germ cells during fetal and postnatal period. *Biol Reprod* **58:** 1250–1256. doi:10.1095/biolreprod58.5.1250

Xu J. 2005. Preparation, culture, and immortalization of mouse embryonic fibroblasts. *Curr Protoc Mol Biol* **70:** 28.1.1–28.1.8. doi:10.1002/0471142727.mb2801s70

Xu J, Wang M, Gao X, Hu B, Du Y, Zhou J, Tian X, Huang X. 2011. Separase phosphosite mutation leads to genome instability and primordial germ cell depletion during oogenesis. *PLoS One* **6:** e18763. doi:10.1371/journal.pone.0018763

Ye Y, Liang Y, Yu Q, Hu L, Li H, Zhang Z, Xu X. 2015. Analysis of human upstream open reading frames and impact on gene expression. *Hum Genet* **134:** 605–612. doi:10.1007/s00439-015-1544-7

Zhang N, Liu FL, Ma TS, Zhang ZZJ. 2019. LncRNA SNHG1 contributes to tumorigenesis and mechanism by targeting miR-338-3p to regulate PLK4 in human neuroblastoma. *Eur Rev Med Pharmacol Sci* **23:** 8971–8983. doi:10.26355/eurrev_201910_19296